

Active and Passive Satellite Observations Coupled with Carbon–Nitrogen Synergy for Urban Fossil Fuel CO₂ Emissions Monitoring

Jinchun Yi ^{#,1}, Yiyang Huang ^{#,1}, Ge Han ^{*,1,3}, Hongyuan Zhang ², Zhipeng Pei ², Haotian Luo ¹, Yichi Zhang¹, Tianqi Shi ⁶, Siwei Li ^{1,3}, Wei Gong ^{4,5}

¹Hubei Key Laboratory of Quantitative Remote Sensing of Land and Atmosphere, School of Remote Sensing and Information Engineering, Wuhan University, Wuhan 430079, China.

²State Key Laboratory of Information Engineering in Surveying, Mapping and Remote Sensing, Wuhan University, Luoyu Road No.129, Wuhan 430079, China.

³Perception and Effectiveness Assessment for Carbon-neutrality Efforts, Engineering Research Center of Ministry of Education, Institute for Carbon Neutrality, Wuhan University, Wuhan, China.

⁴Electronic Information School, Wuhan University, Wuhan, China.

⁵Wuhan Institute of Quantum Technology, Wuhan, China.

⁶Laboratoire des Sciences du Climat et de l'Environnement, LSCE/IPSL, CEA-CNRS-UVSQ, Université Paris-Saclay, 91198 Gif-sur-Yvette, France.

Correspondence to: Ge Han (udhan@whu.edu.cn)

[#] These authors contributed equally to this work.

Abstract. Accurate estimation of fossil fuel CO₂ (ffCO₂) emissions is essential for climate prediction and the development of mitigation policies. Top-down carbon – nitrogen joint observations offer the potential for more reliable ffCO₂ estimates. Here, we establish an inversion framework for urban ffCO₂ emissions based on combined active–passive satellite observations. Urban ffCO₂ distributions were first constructed using satellite NO₂ data and CO₂-NO_x emission ratios, and monthly ffCO₂ emissions for selected global cities were then estimated by integrating the total column dry-air carbon dioxide (XCO₂) from the DQ-1 ACDL instrument. Our results show that satellite-derived NO_x emissions provide strong constraints on urban anthropogenic CO₂ estimates. Validation against TCCON ground-based observations indicates that, compared with conventional top-down inversion approaches, our method more accurately reproduces urban ffXCO₂ plume distributions. We further evaluated the influence of different CO₂-NO_x ratio calculation methods on ffCO₂ estimates and found variations exceeding 150, exerting a substantial impact on emission inversions. Under observational constraints, the uncertainty in CO₂-NO_x ratios derived from different methods decreased by 9.79 – 38.78%, and the variation range was reduced by more than 100%, converging toward a consistent magnitude. This study advances understanding of the spatiotemporal patterns of urban ffCO₂ emissions and provides a unified perspective for future CO₂-NO_x-based anthropogenic carbon emission estimation.

1. Introduction

The intensification of global climate change has driven an increasing demand for high-precision monitoring of fossil fuel CO₂ (ffCO₂) emissions (Agency, 2009). The Paris Agreement emphasizes that countries need rapid and timely access to changes in carbon emissions to support policy formulation and implementation. Achieving this goal relies on accurate and verifiable carbon accounting systems. Cities, due to their high concentration of population, energy consumption, and economic activity, contribute over 70% of global anthropogenic CO₂ emissions, making them key units for evaluating emission reduction policies and compliance monitoring (Crippa et al., 2018). Existing global and regional emission inventories primarily adopt bottom-up statistical accounting methods, estimating emissions based on energy production and sector-specific emission factors (Xu et al., 2024; Wei, 2024). However, these inventories often suffer from significant uncertainties due to data delays and incompleteness (Le Quéré et al., 2018).

To overcome the limitations of bottom-up approaches, top-down atmospheric inversion techniques have advanced rapidly in recent years, enabling constraints on regional carbon budgets. Passive satellite remote sensing systems, such as GOSAT and OCO-2/3, can invert XCO₂ over large portions of the globe and have unique potential for identifying local point sources, estimating regional carbon fluxes, and inferring gross primary productivity (Schwandner et al., 2017; Eldering et al., 2017; Sun et al., 2018b). Nonetheless, top-down inversion methods also rely on accurate prior emission estimates. Inventories that downscale national or regional emissions to high spatial and temporal resolution often suffer from incomplete socio-economic data and inaccurate emission conversion factors, leading to substantial uncertainties in urban emission estimates (Xing et al., 2025; Xu et al., 2025a). Moreover, conventional top-down CO₂ inversion studies have focused primarily on quantifying terrestrial ecosystem carbon fluxes, typically assuming fossil fuel emissions are known and unbiased (Pei et al., 2022). This complicates direct inference of anthropogenic emissions from CO₂ observations due to the atmospheric mixing of fossil fuel and ecosystem fluxes (Ye et al., 2020).

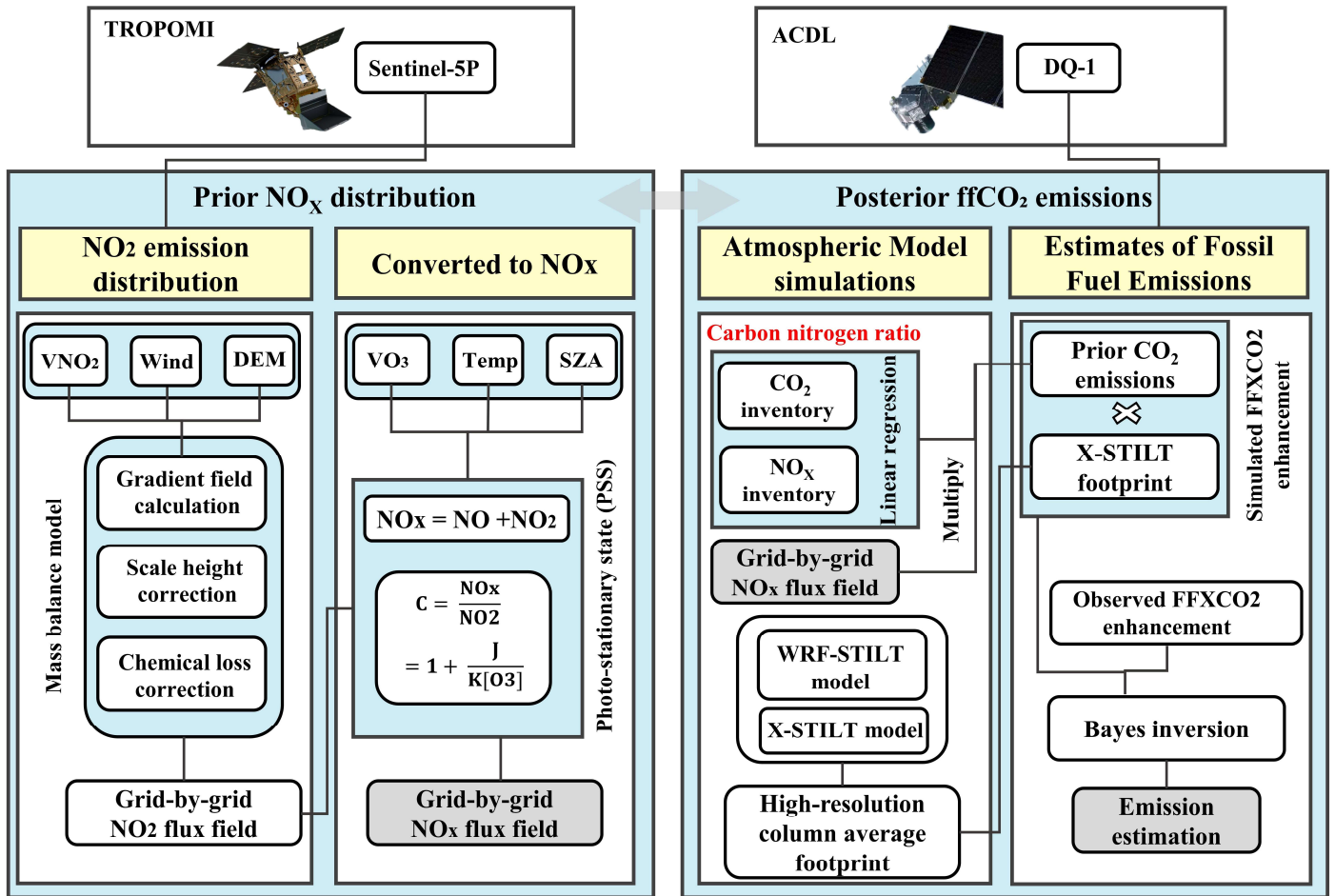
Coupled carbon-nitrogen observations offer a new perspective to address this gap (Reuter et al., 2019; Yang et al., 2023). Nitrogen oxides (NO_x = NO + NO₂) are major co-emitted species from fossil fuel combustion, with emission intensity and spatial distribution closely correlated with ffCO₂ (Feng et al., 2024). Studies have shown that in regions with varying pollution levels, XCO₂ anomalies spatially correlate with tropospheric NO₂ column densities (Hakkarainen et al., 2016). Moreover, the CO₂-to-NO_x ratio is often more stable than individual emission amounts because systematic biases in fossil fuel consumption affect both CO₂ and NO_x statistics (Konovalov et al., 2016). Recent research suggests that optimized NO_x emissions, combined with CO₂-to-NO_x ratios from bottom-up inventories, can provide more accurate ffCO₂ estimates (Zheng et al., 2020). For instance, Zheng et al. used TROPOMI NO₂ data to estimate 10-day moving averages of Chinese ffCO₂ emissions during the COVID-19 pandemic, finding an 11.5% decline compared to the same period in 2019 (Zheng et al., 2020). Liu et al. validated the feasibility of NO_x-based ffCO₂ estimation by comparing inferred CO₂ emissions with highly accurate stack measurements from eight large US power plants (Liu et al., 2020). High-resolution NO₂ column observations, such as those from Sentinel-5P/TROPOMI, can be inverted using a mass-balance

60 framework to derive accurate NO_x gridded fluxes(Qin et al., 2023; Sun, 2022). These NO_x fluxes can inform the prior spatial
61 allocation of CO_2 emissions due to the co-emission consistency of fossil fuel sources, and the high temporal resolution of TROPOMI
62 allows rapid updates of CO_2 priors, mitigating the lag inherent in static inventories(Zhang et al., 2022).

63 The CO_2 -to- NO_x ratio is crucial for converting NO_x emissions into ffCO_2 estimates. However, because the CO_2 -to- NO_x ratio
64 used in this study is calculated from CO_2 emissions and NO_x emissions, there is currently a lack of accurate top-down measurement
65 methods, most studies derive this ratio from inventories, and different calculation methods yield significantly different values.
66 Assimilating observational data to invert CO_2 -to- NO_x ratios is therefore key to reducing uncertainties in ffCO_2 estimation. Passive
67 top-down observations are limited by cloud cover, aerosols, and solar irradiance, and in complex multi-source and topographic
68 environments, signal attribution is challenging, restricting the accuracy and stability of city-scale inversions(Miller et al., 2014; Han
69 et al., 2026).

70 In 2022, China launched DQ-1, the world's first CO_2 lidar satellite, equipped with an IPDA lidar (ACDL) capable of high
71 signal-to-noise ratio, day-and-night, all-weather observations. The dual-wavelength differential method mitigates interference from
72 aerosols and thin clouds(Han et al., 2025). Compared to passive satellites, IPDA lidar offers unique advantages in urban plume
73 detection and fine-scale emission inversion(Kiemle et al., 2017; Zhang et al., 2026). Previous studies using DQ-1 XCO_2 data
74 successfully constrained point-source emissions(Cheng et al., 2025; Han et al., 2024; Zhang et al., 2025), and Yi et al. developed a
75 kilometer-scale urban flux inversion system based on ACDL measurements, comparing its constraints to passive systems like OCO-
76 2/3(Yi et al., 2025).

77 In this study, we propose a city-scale ffCO_2 inversion framework that jointly assimilates active and passive satellite observations,
78 dynamically bridging NO_x and CO_2 emissions via the CO_2 -to- NO_x ratio. The workflow is illustrated in Fig. 1. TROPOMI NO_2
79 column data are first used to invert NO_x gridded emissions via a mass-balance approach. Combined with prior CO_2 -to- NO_x ratios,
80 these NO_x fluxes are converted into CO_2 priors. DQ-1 XCO_2 -Lidar along-track measurements are then assimilated using WRF-
81 STILT high-resolution atmospheric transport simulations within a Bayesian inversion framework to estimate total city emissions
82 and explicitly quantify observational and transport uncertainties. We applied this approach to Beijing, Paris, and Cairo, representing
83 cities with diverse topographies and emission patterns, using August 2022 TROPOMI and DQ-1/ACDL data to evaluate the
84 framework's ability to provide robust, high-resolution urban emission estimates. It is noteworthy that no unified CO_2 -to- NO_x ratio
85 calculation method currently exists, and different methods yield divergent values, which can significantly bias final emission
86 estimates. This study systematically evaluates the influence of prior CO_2 -to- NO_x ratio calculation methods on inversion outcomes,
87 demonstrating that Bayesian assimilation can substantially reduce this uncertainty, converging different ratios to a consistent
88 magnitude. This framework offers a unified approach for estimating urban emissions under limited or uncertain inventory conditions,
89 providing a timely and reliable method for reporting anthropogenic CO_2 emissions at the city scale.



90
91 **Figure 1 Technical framework diagram**

92 The remainder of this paper is structured as follows. Section 2 introduces the datasets and methods used in this study. Section
93 3 presents the results of NO_x emission estimation in Paris, Cairo, and Beijing based on TROPOMI observations combined with a
94 mass-balance approach, followed by city-scale ffCO₂ inversion results obtained by assimilating DQ-1 ACDL observations within a
95 Bayesian framework. Section 4 examines the influence of different prior CO₂-to-NO_x ratio calculation methods on the inversion
96 process and highlights the importance of optimizing the CO₂-to-NO_x ratio using observational data. Finally, Section 5 summarizes
97 and discusses the potential of the multi-source satellite Bayesian inversion framework for constraining urban CO₂ emissions, and
98 emphasizes the significance of optimized CO₂-to-NO_x ratios for improving the accuracy of urban ffCO₂ estimates.

99 **2. Materials and methods**

100 **2.1. Data**

101 **2.1.1. ACDL Productions**

102 The concept of DQ-1 was first proposed in 2012 with the aim of developing a satellite-borne lidar system analogous to the
103 Cloud-Aerosol Lidar with Orthogonal Polarization (CALIOP) onboard CALIPSO, and it was officially approved as a national

project in 2017(Zhang et al., 2024). Unlike conventional environmental monitoring satellites, DQ-1 is distinguished by its breakthrough active remote sensing payload—the Atmospheric Carbon Dioxide Differential Absorption Lidar (ACDL)—which enables active “top-down” observations of atmospheric CO₂(Zhang et al., 2023). The ACDL underwent successive stages of laboratory prototype development and airborne validation before its successful launch onboard the DQ-1 satellite into a near-polar sun-synchronous orbit at an altitude of ~705 km on April 18, 2022. Operational observations commenced in late May of the same year. This study primarily analyzes data collected August 2022.

The ACDL operates on the principle of Integrated Path Differential Absorption (IPDA) lidar, retrieving atmospheric column-averaged CO₂ concentrations (X_{CO_2}) via differential absorption techniques. The inversion methodology and data product specifications have been described in detail elsewhere; here, we provide only a brief overview(Han et al., 2025). The instrument transmits two nearly simultaneous laser pulses: one at a strong absorption line of CO₂ (R16, referred to as the “online” wavelength) and the other at a nearby weak absorption line (the “offline” wavelength). These are stabilized at 6361.225 cm⁻¹ and 6360.981 cm⁻¹, corresponding to 1572.024 nm and 1572.085 nm, respectively. By comparing the differential attenuation between the online and offline signals, the system effectively mitigates the influence of aerosols and other interfering species, except water vapor, thereby enabling accurate retrievals of X_{CO_2} . The inversion process relies on dedicated algorithms, with the central concept being that the small wavelength offset produces differential absorption, which enhances the sensitivity of CO₂ detection (details of the ACDL X_{CO_2} retrieval algorithm are provided in the Appendix A1).

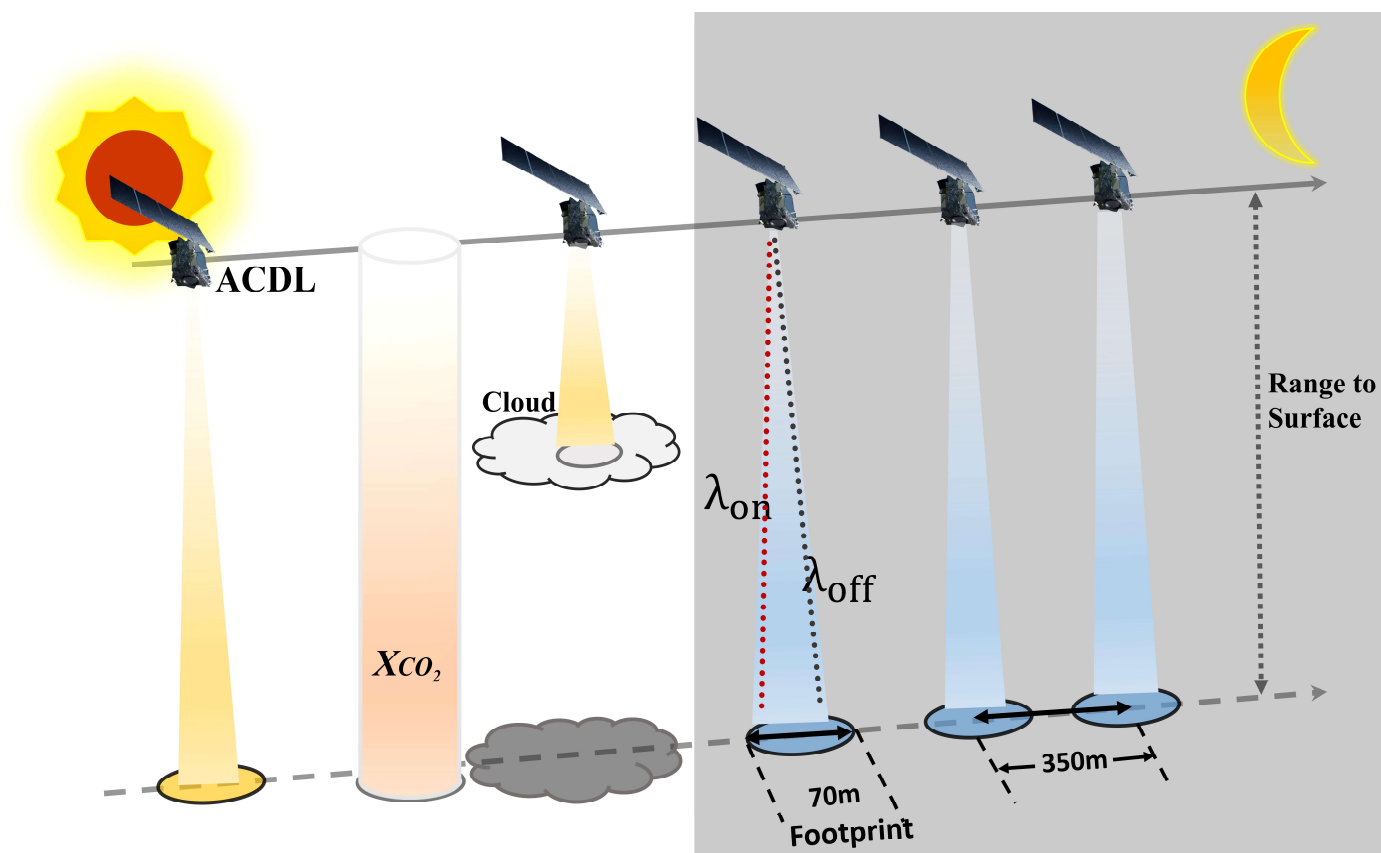


Figure 2 the schematic diagram for DQ-1's detection principle

122
123 Figure 2 illustrates the schematic of the DQ-1 measurement principle. The XCO₂ products generated by ACDL are provided in
124 a point-sampling mode analogous to that of GOSAT. The lidar records one footprint of approximately 70 m every ~350 m along the
125 satellite ground track. Additional details of the ACDL operating parameters are provided in the Appendix A1.

126 **2.1.2. TROPOMI Productions**

127 TROPOMI is a nadir-viewing spectrometer onboard ESA's Sentinel-5 Precursor (S5P) satellite, which was launched in October
128 2017. Operating in an ascending Sun-synchronous polar orbit with an equator crossing time of approximately 13:30 local time,
129 TROPOMI measures a range of trace gases as well as cloud and aerosol properties across four spectral channels (ultraviolet, visible,
130 near-infrared, and shortwave infrared). The instrument's minimum pixel size was about 3.5×7 km² at nadir before being reduced
131 to $\sim 3.5 \times 5.5$ km² on 6 August 2019 (Veefkind et al., 2012). In this study, we used the S5P-PAL dataset (consistent with version
132 2.3.1) (Eskes et al., 2021) covering the period from 1 August to 1 September 2022, obtained from <https://data-portal.s5p-pal.com>

133 To ensure data quality, we filtered out pixels with a qa_value < 0.75 (Qin et al., 2023), and, following van Geffen et al., removed
134 cloudy pixels (cloud radiance fraction > 50%) as well as anomalies (e.g., eclipses) from the TROPOMI NO₂ dataset (Van Geffen et
135 al., 2022). To test our algorithm framework on a robust dataset, we selected summer NO₂ observations for three cities located in the
136 mid-latitudes of the Northern Hemisphere, avoiding winter measurements that may be complicated by potential snow cover.
137 Furthermore, given the need for city-scale accuracy, air mass factor (AMF) corrections were applied locally following the method
138 described in (Beirle et al., 2023).

139 Sun et al. proposed an oversampling algorithm to project multi-satellite, multi-species observations onto a common grid, with
140 code publicly available on GitHub (https://github.com/Kang-Sun-CfA/Oversampling_matlab/) (Sun et al., 2018a). In this work, we
141 applied this algorithm to the pre-processed TROPOMI overpass data, generating oversampled grids at 1 km resolution following
142 the procedure described in (Sun, 2022).

143 **2.1.3. Meteorological and DEM data**

144 For the estimation of CO₂ emissions through model simulations, we utilized meteorological parameters from the National
145 Centers for Environmental Prediction Final (NCEP FNL) operational global analysis dataset (National Centers for Environmental
146 Prediction/National Weather Service/NOAA/U.S. Department of Commerce, 2015). The ds083.3 dataset is provided on a $0.25^\circ \times$
147 0.25° latitude–longitude grid and updated every six hours via the Global Data Assimilation System (GDAS)
148 (<https://rda.ucar.edu/datasets/ds083-3/>). It covers 32 vertical levels, ranging from the surface to the top of the atmosphere, including
149 the ground level and 31 isobaric layers from 1000 hPa to 1 hPa. Essential variables such as surface pressure, geopotential height,
150 temperature, relative humidity, and zonal and meridional wind components were used as the main meteorological inputs for driving

151 the WRF-STILT simulations.

152 The wind vector data were obtained from the ERA5 reanalysis dataset (<https://doi.org/10.24381/cds.adbb2d47>)(Hersbach et
153 al., 2023). We extracted hourly 10 m and 100 m wind vectors at 0.25° spatial resolution for the three selected cities during the period
154 from 1 August to 1 September 2022. The 10 m wind vectors are used to approximate near-surface winds, whereas the 100 m wind
155 vectors represent horizontal transport within the planetary boundary layer. These data were averaged to daily values and
156 subsequently interpolated to match the grid resolution of the column concentration fields described in Section 2.3.1.

157 Digital elevation data were obtained from the GMTED2010 dataset (<https://www.usgs.gov/coastal-changes-and-impacts/gmted2010>)(Danielson and Gesch, 2011). The DEM was resampled and mapped to the same spatial grid as the
158 concentration and wind fields to ensure consistency across all datasets.
159

160 **2.1.4. Emissions Inventory**

161 In this study, multiple emission inventories were used to estimate fossil fuel CO₂ (ffCO₂) emissions and to calculate the CO₂-
162 to-NO_x ratio. In the urban observation system simulation experiment (Section 3), the GEMS inventory (0.1° resolution) for NO_x and
163 CO₂ emissions(Huang et al., 2017) was used to derive the prior CO₂-to-NO_x ratio (available at: <https://gems.sustech.edu.cn/data>).
164 For comparison, we also employed the gridded fossil fuel CO₂ emissions inventory from the Open - source Data Inventory for
165 Atmospheric Carbon dioxide (ODIAC, Version 2024, 1 km resolution; <https://db.cger.nies.go.jp/dataset/ODIAC/>). In Section 4, we
166 further utilized the sectoral and 0.1° gridded NO_x and CO₂ inventories from the Emissions Database for Global Atmospheric
167 Research (EDGAR; https://edgar.jrc.ec.europa.eu/emissions_data_and_maps)(Crippa et al., 2018), as well as the sectoral NO_x and
168 CO₂ inventories from the Multi-resolution Emission Inventory model for Climate and air pollution research (MEIC;
169 <http://meicmodel.org.cn/>)(Team, 2012). Using different approaches to calculate the CO₂-to-NO_x ratio, we quantified the variations
170 arising from different inventory inputs and assessed their impact on emission inversions.

171 **2.2. Methodology**

172 **2.2.1. Calculation of Prior Distribution for CO₂ Emissions**

173 **(1) Mass Balance Method**

174 In previous studies, numerous works have detailed the theoretical derivation for inferring gridded fluxes from column
175 observations(Huang et al., 2024; Koene et al., 2024; Qin et al., 2023; Rey-Pommier et al., 2025; Sun, 2022). Such frameworks are
176 generally based on solutions to the atmospheric continuity equation. Divergence-based approaches typically rely on several key
177 assumptions: (1) exchanges above the planetary boundary layer (column top) and at the surface (column bottom) are neglected,
178 effectively assuming two-dimensional diffusion; (2) horizontal turbulent transport is ignored at coarse grid resolutions; and (3) the

deposition term S is treated using a first-order chemical approximation. Starting from the unsteady, source-driven atmospheric continuity equation, the gridded flux of a given species, such as NO_2 , can be derived from satellite column observations, with the resulting flux $\langle E_{\text{NO}_2} \rangle$ expressed as in Equation 1.

$$\langle E_{\text{NO}_2} \rangle = \langle \vec{u} \cdot (\nabla V_{\text{NO}_2}) \rangle + \frac{\langle V_{\text{NO}_2} u_{10} \cdot (\nabla z_0) \rangle}{H} + \frac{\langle V_{\text{NO}_2} \rangle}{\tau} \quad (1)$$

The detailed derivation is provided in Appendix A2. To fully exploit the available data while accounting for observational errors, spatial gradients were computed along the zonal, meridional, and both diagonal directions. Gradients were numerically approximated using second-order central differences, multiplied by the corresponding decomposed wind vectors, and then averaged. For boundary grid points, one-sided differences were applied. Although using gradients in multiple directions helps reduce directional dependence, the finite-difference gradient operator can amplify high-frequency retrieval noise in the original NO_2 column field. Therefore, the divergence-derived NO_x fluxes should not be interpreted as purely deterministic grid-cell emissions. Instead, they represent monthly aggregated estimates subject to retrieval noise, wind-field uncertainty, chemical-parameter uncertainty, and possible structured errors introduced by gradient operations and gridding. We further evaluate this sensitivity in Appendix A5.

(2) Convert NO_2 to NO_x

Nitrogen oxides ($\text{NO}_x = \text{NO} + \text{NO}_2$) do not exist independently in the troposphere, as NO and NO_2 continuously interconvert, while the total NO_x remains relatively stable. To convert between NO_2 column densities and total NO_x columns, Sun et al. applied a fixed coefficient of 1.32. In this study, we adopt a more rigorous approach to derive the conversion factor, as expressed in Equation 2 (Beirle et al., 2023), based on the photostationary steady-state assumption:

$$\begin{cases} V_{\text{NO}_x} = \alpha V_{\text{NO}_2} = \left(1 + \frac{J}{K X_{\text{O}_3}}\right) V_{\text{NO}_2} \\ J = k_1 * \exp\left(-\frac{k_2}{\cos(\text{SZA})}\right) \\ K = k_3 * \exp\left(-\frac{k_4}{T}\right) \end{cases} \quad (2)$$

Here, J represents the photolysis frequency of NO_2 , calculated following the methodology in (Dickerson et al., 1982). The rate constants k_1 and k_2 are set to 0.0167 and 0.575, respectively. The solar zenith angle (SZA) can be directly determined from the local latitude, longitude, and time; in this study, SZA values are obtained from the TROPOMI satellite metadata. K denotes the chemical reaction rate constants for NO with O_3 , expressed in $\text{cm}^3/(\text{mol} \cdot \text{s})$ and recommended by IUPAC, with $k_3=2.07 \cdot 10^{-12}$ and $k_4=1400$. The ozone mixing ratio, X_{O_3} , is derived from the ESCiMo project (Brenninkmeijer and Cai, 2016), and T represents the boundary-layer mean temperature obtained from ERA5 reanalysis data. Under these definitions, Equation 2 can be rewritten as:

$$X = \alpha * \langle E_{\text{NO}_2} \rangle \quad (3)$$

Using Equation 3 we can obtain grid-resolved estimates of NO_x fluxes, which serve as the prior distribution for fossil fuel CO_2

(ffCO₂) emissions. These estimates provide a data-driven prior inventory for subsequent steps in the inversion framework.

(3) Scale height and Chemical lifetime

Regarding the selection of scale height and first-order chemical lifetime, previous studies, such as Beirle et al., employed fixed empirical scale height values and adjusted terrain correction terms to obtain optimal estimates(Beirle et al., 2023). Their chemical lifetime was calculated using a compensation method that accounted for losses integrated over residence times within a 15 km buffer. While effective at point-source scales, this approach is not directly applicable to our study. In the present work, we follow Sun et al.'s purely data-driven approach, which leverages observational data without introducing additional assumptions, constructing a linear regression model to determine these parameters(Sun, 2022). This observation-driven fitting method not only reduces errors arising from new assumptions but also mitigates biases caused by grid resampling and near-surface wind selection.

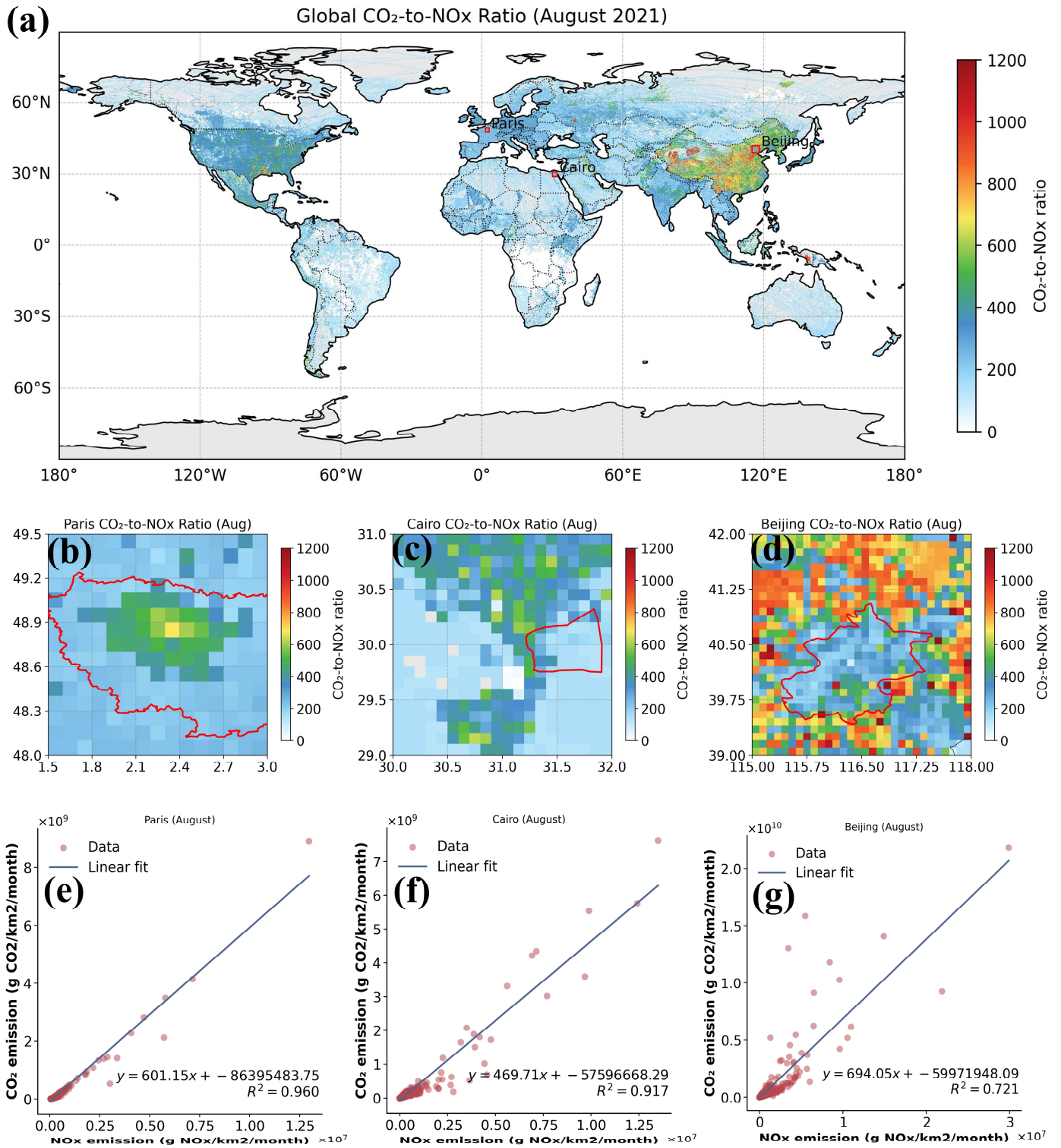
To suppress excessive noise in single-day fits, we perform monthly regressions and adopt the temporal and spatial mean over the month as the final estimate, representing an aggregate over the full spatial domain, the entire month, and the troposphere. The retrieved scale height and first-order chemical lifetime are then applied back into Equations 4 and 6 to obtain the final gridded NO_x vertical fluxes.

After terrain correction, the gridded flux fields remove a substantial portion of strong emission signals obscured by wind divergence and negative divergence artifacts, while the chemical correction term adjusts residual minor negative biases(Sun, 2022; Beirle et al., 2023). Any remaining small negative values after these corrections are set to zero.

(4) Calculation of Prior CO₂-to-NO_x Ratio

We used the prior CO₂-to-NO_x ratio in combination with TROPOMI-derived NO_x emission distributions to obtain an initial characterization of urban prior ffCO₂ emissions. Following the approach of Feng et al., who calculated the CO₂-to-NO_x ratio by dividing gridded CO₂ and NO_x emission inventories(Feng et al., 2024), we derived city-specific prior CO₂-to-NO_x ratio using the 0.1° CO₂ and NO_x inventories from GEMS (<https://gems.sustech.edu.cn/data/database>). Unlike Feng et al., who focused on grid-level CO₂-to-NO_x ratio, we fitted the gridded ratios across each study region to obtain an integrated city-level CO₂-to-NO_x ratio, which is more suitable for subsequent inversion analyses (Fig. 3). Details on the associated uncertainties are provided in Section 4.1.

Figure 3 illustrates our method for calculating the prior CO₂-to-NO_x ratio. By fitting the 0.1° gridded ratios for each city, we obtained overall city-scale values. The coefficients of determination (R²) for Paris, Cairo, and Beijing were 0.96, 0.917, and 0.76, respectively.



233
 234 **Figure 3** Schematic diagram of prior CO₂-to-NO_x ratio calculation methods. Panel (a) shows the global gridded CO₂-to-NO_x ratio derived
 235 from GMES data. Panels (b)–(d) present the gridded CO₂-to-NO_x ratio for Paris, Cairo, and Beijing (the red lines indicate the boundaries
 236 of each city). Panels (e)–(g) display the overall CO₂-to-NO_x ratio fitting results for the three cities. We used the Île-de-France administrative
 237 boundary to depict Paris in the figures, rather than the city proper. Although our actual study area only covers a subset of Île-de-France
 238 (1.5–3° E, 48–49.5° N)

239 Recently, an increasing number of studies have employed NO_x emissions to estimate ffCO₂ emissions(Feng et al., 2024; Zheng
 240 et al., 2020; Xu et al., 2025b; Yang et al., 2023; Zhang et al., 2022). In inversion methods based on NO_x emissions, the choice of the

241 prior CO₂-to-NO_x ratio directly affects the emission estimates. Uncertainty in the prior ratio propagates to the estimated ffCO₂
242 emissions, influencing both their magnitude and spatial distribution. To evaluate this effect, we selected several widely used CO₂-
243 to-NO_x ratio calculation methods and systematically assessed their associated uncertainties (results see Section 4.1 and Appendix
244 A6).

- 245 - M.1 Grid-level CO₂-to-NO_x ratio derived directly from gridded CO₂ and NO_x inventories(Feng et al., 2024). Since this study
246 scales emissions to the city level, we further fitted the grid-level ratios to obtain city-integrated CO₂-to-NO_x ratios. M.1
247 calculations were based on the GEMS gridded inventory.
- 248 - M.2 CO₂-to-NO_x ratios calculated using sectoral emission factors for CO₂ and NO_x(Zheng et al., 2020). We derived city-scale
249 ratios by aggregating across all sectors. M.2 used the GEMS sectoral emission factors.
- 250 - M.3 CO₂-to-NO_x ratios derived from near-real-time satellite observations. Background-stable NO_x plumes were used to
251 constrain CO₂ plumes, and joint fitting of the two concentrations was performed using the cross-sectional flux method(Xu et
252 al., 2025b; Reuter et al., 2019). The CO₂-to-NO_x ratio was obtained directly from the half-width at half-maximum. Following
253 this approach, we used TROPOMI and OCO-2 observations to calculate city-scale ratios.
- 254 - M.4 Same as M.2, but the MEIC sectoral inventory was used for Beijing.
- 255 - M.5 Same as M.1, but calculations were based on the EDGAR gridded inventory.
- 256 - M.6 Same as M.2, but calculations were based on the EDGAR sectoral inventory.

257 2.2.2. Estimating ffCO₂ emissions by WRF-STILT simulations

258 (1) Quantifying ffXCO₂ enhancements

259 Distinguishing anthropogenic emission signals from the surrounding “clean” background in XCO₂ observations is a central
260 challenge for constraining urban carbon emissions via satellite. Definitions of “background” vary across studies. In this work, we
261 define the background as atmospheric XCO₂ that is unaffected by local emissions within the study region. Following the approach
262 proposed by (Ye et al., 2020)in constraining urban emissions using OCO-2 observations, we adopt a baseline calculation strategy
263 that incorporates latitudinal gradients.

264 In this framework, XCO₂ is decomposed into two components: $XCO2_{trend}$, representing the regional-scale, non-local trend,
265 and $XCO2_{local}$, whose standard deviation σ_{local} characterizes local-scale variability. Samples satisfying $XCO2 < XCO2_{trend} +$
266 $0.5\sigma_{local}$ are selected as “background samples,” as they exhibit lower local spatial variability compared with data influenced by
267 fossil fuel emissions. These background samples are then subjected to linear regression to derive the background baseline and
268 characterize its spatial variation.

269 (2) X-Stochastic Time-Inverted Lagrangian Transport model for ACDL productions

270 We employ the X-STILT V1 model to trace CO₂ concentration variations driven by prior emission information. X-STILT
 271 integrates satellite profile data and enables a comprehensive uncertainty assessment of urban XCO₂ enhancements on a per-
 272 observation basis (Wu et al., 2018). Originally developed to extract urban signals from passive OCO-2 XCO₂ observations, we have
 273 adapted the framework for use with the active CO₂ satellite DQ-1, with appropriate modifications. The relationship between
 274 XCO₂^{Lidar} (DQ-1 XCO₂ observations) measurements and the CO₂ vertical profile, CO₂(p), can be formulated as follows:

$$275 \quad XCO_2^{Lidar} = \frac{\int_{p_{surface}}^{p_{toa}} CO_2(p) WF(p) dp}{\int_{p_{surface}}^{p_{toa}} WF(p) dp} = \sum_{n=1}^{toa} \frac{WF(p_n)}{IWF} \cdot CO_2(p_n) \quad (4)$$

276 Here, p_{toa} represents the pressure at the bottom height of the ACDL, and $p_{surface}$ represents the pressure corresponding
 277 to the surface elevation at the laser footprint. WF and IWF denote the weighting function and the normalized weighting function
 278 of the ACDL, respectively. A detailed description is provided in Appendix A1.

279 We approximate the CO₂ concentration by summing the background concentration with the simulated ffCO₂ enhancement.
 280 Here, the simulated ffCO₂ enhancement, $\Delta CO_2_{ffCO_2}(p) = \langle ffCO_2, foot(p) \rangle$, is obtained by interpolating the modeled ffCO₂
 281 fluxes along tracer-tagged footprints. Consequently, the relationship between the ffCO₂ fluxes and the simulated $XCO_2^{Lidar}_{mod}$, is
 282 established, yielding the modeled fossil fuel CO₂ enhancement $XCO_2^{Lidar}_{ffCO_2, mod}$ along the lidar track:

$$283 \quad XCO_2^{Lidar}_{ffCO_2, mod} = XCO_2^{Lidar}_{mod} - XCO_2^{Lidar}_{background} = \sum_{n=1}^{toa} \frac{WF(p_n)}{IWF} \cdot \langle emissions, foot(p_n) \rangle \quad (5)$$

284 $XCO_2^{Lidar}_{background}$ represents the background concentration along the selected DQ-1 orbit (see Section 2.2.2 (1)). The operator
 285 \langle, \rangle denotes an inner product, $emissions$ is the prior emission flux, and $foot(p_n)$ represents the modeled footprint at different
 286 vertical layers. Using the above formulation, the mathematical foundation for the inversion is established. By integrating footprints
 287 across multiple release heights, the equation can be further simplified. In this study, we define the ffXCO₂ enhancement simulated
 288 via the atmospheric transport model as:

$$289 \quad XSTILT^{Lidar} = \sum_{n=1}^{toa} \frac{WF(p_n)}{IWF} \cdot foot(h_n) \quad (6)$$

$$290 \quad XCO_2^{Lidar}_{ffCO_2, mod} = \langle XSTILT^{Lidar}, emissions \rangle \quad (7)$$

291 Here, $XSTILT^{Lidar}$ is defined as the column-averaged footprint, corresponding to the column-averaged CO₂ concentration.
 292 The inner product of the column-averaged footprint and the prior emission flux yields the simulated XCO₂ enhancement.

293 (3) Bayes inversion

294 We used the NO_x emissions obtained previously as prior fluxes and, through the CO₂-to-NO_x ratio, established the relationship

between the prior emissions and the XCO₂ observed by DQ-1 (Equation 9). The XCO₂ enhancements estimated from DQ-1 observations were then employed to impose “top-down” constraints on the simulated results. Following the approaches of (Che et al., 2024; Ye et al., 2020; Sheng et al., 2025), we applied a Bayesian inversion framework to optimize the prior emission estimates.

$$y_{obs} = y_{sim} \cdot \lambda + \varepsilon_p \quad (8)$$

Here, y_{obs} and y_{sim} represent the observed ffXCO₂ enhancements and the simulated NO_x enhancements, respectively. The symbol λ denotes the CO₂-to-NO_x ratio, and ε_p represents the observational error, which encompasses contributions from DQ-1 measurement uncertainties, model errors, and errors in model parameters. It is defined as follows:

$$\begin{cases} y_{obs} = \int_{latitude1}^{latitude2} ffXCO2_{obs} dt \\ y_{sim} = \int_{latitude1}^{latitude2} < X, footprint > dt \end{cases} \quad (9)$$

$$\varepsilon_{obs} = \sqrt{\sigma_{measurement}^2 + \sigma_{sim}^2} \quad (10)$$

In this context, ffXCO_{2,obs} represents the DQ-1 XCO₂ enhancement after background concentration removal. The notation $< X, footprint >$ denotes the simulated NO_x enhancement, obtained by convolving the NO_x emission inventory X with the STILT-derived footprint (It should be noted that the footprints used here represent hourly footprints during the simulation period, whereas the NO_x emissions are monthly emissions derived using the method described in Section 2.2.1. Therefore, we use the New High Resolution Temporal Profiles in EDGAR dataset (https://edgar.jrc.ec.europa.eu/dataset_temp_profile) to distribute the monthly NO_x emissions to each hourly footprint). Pseudo-observations, ffXCO_{2,obs}, are generated by averaging DQ-1 measurements over one-second intervals along the satellite track (~7 km), together with the corresponding simulated values.

Following the Bayesian inversion approach, the state vector λ is expressed in terms of the CO₂-to-NO_x ratio, representing the relationship between urban fossil fuel CO₂ and NO_x emissions. The Jacobian matrix is derived from the simulated NO_x enhancement y_{sim} . Here, $\sigma_{measurement}^2$ represents the observational error variance, and σ_{sim}^2 denotes the model transport error variance. DQ-1 observations are assumed unbiased with respect to the true state. To account for measurement uncertainty, random Gaussian noise with a standard deviation of 0.3 ppm—representing the lower limit of observational error—is added to the observations.

By minimizing the loss function, we obtain the posterior CO₂-to-NO_x ratio $\hat{\lambda}$ and posterior uncertainty $\hat{\sigma}$:

$$\hat{\lambda} = \lambda + \sigma_{sim}^2 y_{sim}^T (y_{sim} S_{obs} y_{sim}^T + S_{obs})^{-1} (y_{obs} - y_{sim} \lambda) \quad (11)$$

$$\hat{\sigma}^2 = (y_{sim}^T S_{obs}^{-1} y_{sim} + \sigma_{sim}^{-2})^{-1} \quad (12)$$

Here, S_{obs} is a diagonal matrix, with the diagonal entries representing the observational error variances ε_{obs}^2 for each orbit. the prior uncertainty σ_{sim} is primarily derived from the uncertainties in the prior NO_x emission distribution σ_{NOx} and the prior

CO₂-to-NO_x ratio $\sigma_{C/N}$ as equation 13:

$$\sigma_{sim} = \sqrt{\sigma_{NO_x}^2 + \sigma_{C/N}^2} \quad (13)$$

3. Urban Observation System Simulation Experiment

3.1. Satellite-driven urban NO_x emission distribution

As described in Section 2.2.1, we applied the mass balance approach in the three cities to derive prior NO_x gridded inventories, which serve as the basis for constructing ffCO₂ gridded emissions. The grid resolution was set to 5 km × 5 km. Figure 4 illustrates the detailed NO_x fluxes for August 2022 over Beijing, Paris, and Cairo, produced entirely via a top-down approach, with panels (a)–(c) corresponding to Beijing, Paris, and Cairo, respectively.

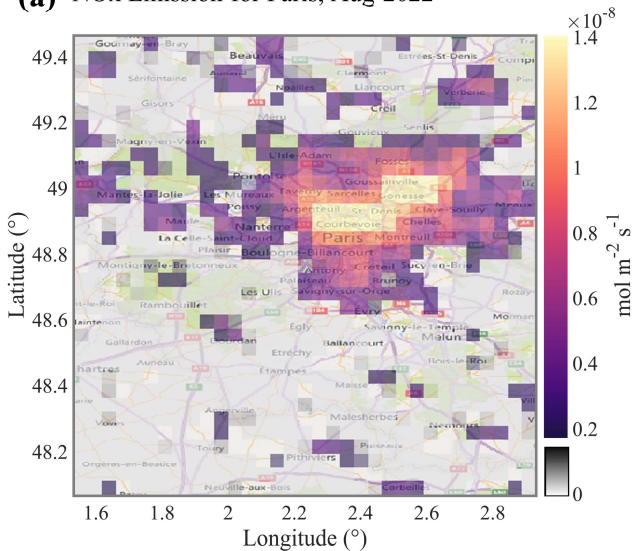
From the figure, it is evident that the average NO_x flux magnitude in all three cities is on the order of $\sim 10^{-8}$ mol m⁻² s⁻¹. However, their spatial distributions differ considerably. Both Paris and Cairo exhibit highly concentrated emission patterns. In Cairo, the central urban area and industrial zones display peak NO_x fluxes on the order of $\sim 10^{-7}$ mol m⁻² s⁻¹. These high-flux regions sharply decrease with distance from the center, highlighting a pronounced urban boundary effect (Li et al., 2025). In contrast, Beijing not only exhibits strong emissions in the central urban area (within the Sixth Ring Road) but also features numerous dispersed point- and area-like sources in suburban districts (e.g., Fangshan in the southwest) and in the surrounding hills and mountains. Compared with Cairo’s concentrated emissions, Beijing’s peak NO_x grid flux in the urban core is nearly one order of magnitude lower (see the color scale mapping in Fig. 4); however, due to the city’s larger spatial extent, the total flux remains substantially higher than that of Cairo.

Beijing’s topography, with higher elevations in the northwest and lower elevations in the southeast, can induce local wind divergence over hilly and mountainous areas. This effect may generate false positives when using the divergence method (Sun et al., 2021; Liu et al., 2021). In the northwestern suburban mountains of Beijing, the mean wind divergence can reach magnitudes of $\sim \pm 10^{-4}$ s⁻¹, while TROPOMI NO₂ column densities are on the order of 10⁻⁴ mol m⁻². Such magnitudes are comparable to mid-scale urban averages or point-source emissions. Neglecting the divergence term can result in genuine emissions being omitted, while background fluxes induced by terrain or wind divergence are mistakenly included. Following (Sun, 2022), we applied Eq. A5 to reconstruct the wind-divergence term using surface wind and terrain gradients, thereby reintegrating previously neglected area-like emissions. Using Beirle et al.’s methodology, we integrated the net gridded fluxes within a 60 km radius centered on Beijing over the entire year of 2022 to estimate the city’s annual NO_x emissions at 251,450 t. This value is approximately 9.7% higher than the 2022 annual emission reported in the MEIC inventory for Beijing (227,000 t). Although the total magnitude is consistent, the spatial distribution from top-down estimates differs substantially from bottom-up inventories. Section 3.2.2 further analyzes these

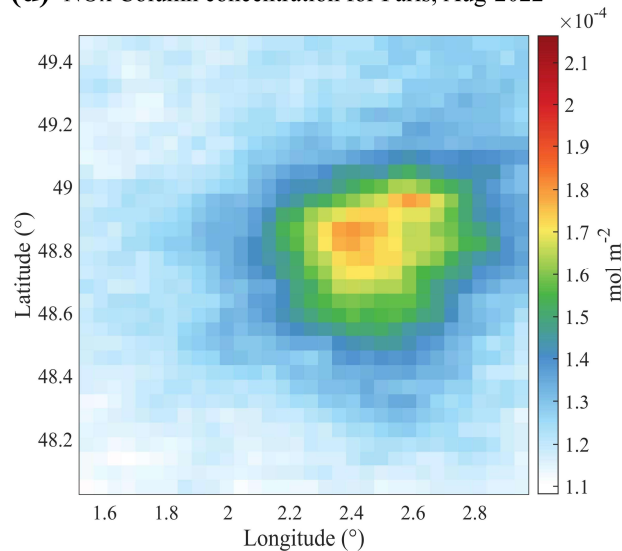
349 differences by simulating urban ffCO₂ plumes using both our ffCO₂ inventory and the ODIAC inventory.

350 By comparison, Paris and Cairo are situated on relatively flat terrain (maximum elevation ~180 m). Terrain-induced wind
351 divergence is negligible relative to total fluxes (wind-terrain and divergence contributions $\sim 10^{-10}$ mol m⁻² s⁻¹), leaving the continuity
352 equation primarily governed by wind-weighted column gradients. Cairo, located upstream of the Nile Delta in a high-albedo desert
353 region, benefits from low uncertainty in satellite-derived NO₂ columns. Under these conditions, the top-down NO_x inventory closely
354 aligns with the bottom-up inventory in terms of spatial distribution. Paris, situated in the Paris Basin along the Seine River,
355 experiences minimal terrain gradients. Although less extreme than Cairo, the slight topographic variation still produces pronounced
356 urban boundary effects in the inversion results.

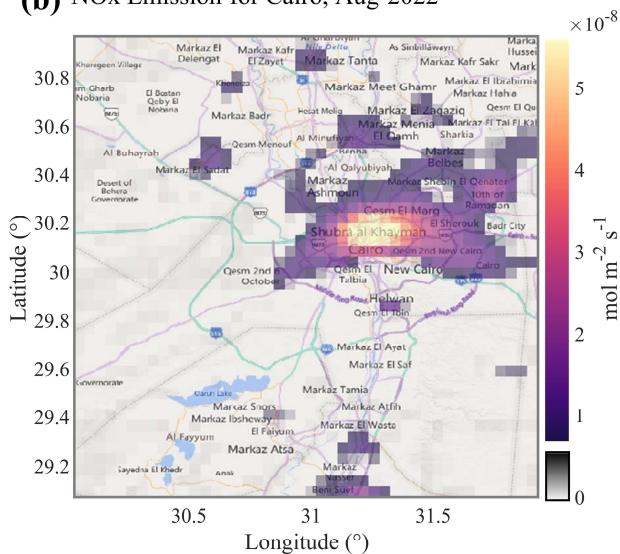
(a) NO_x Emission for Paris, Aug-2022



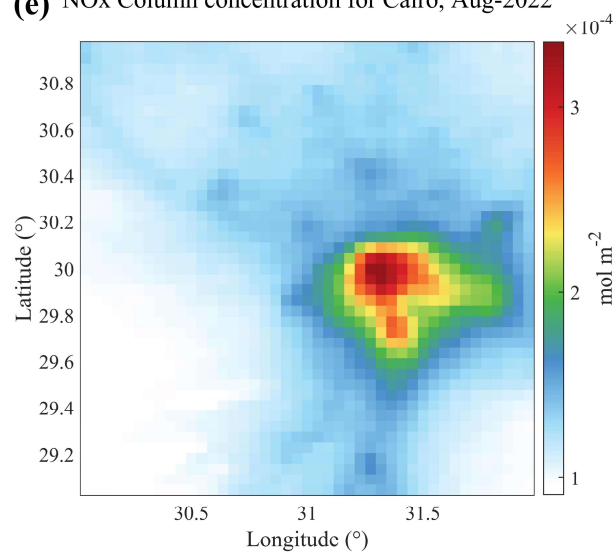
(d) NO_x Column concentration for Paris, Aug-2022



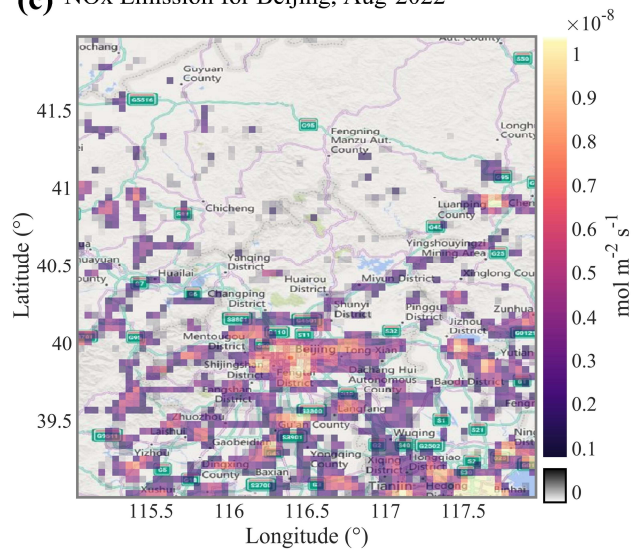
(b) NO_x Emission for Cairo, Aug-2022



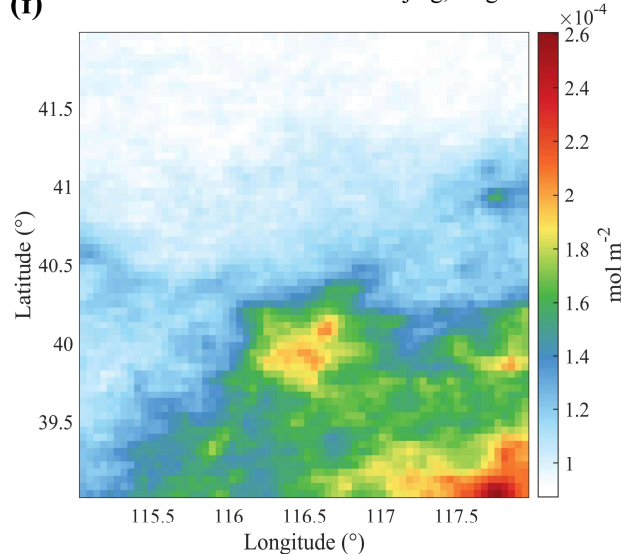
(e) NO_x Column concentration for Cairo, Aug-2022



(c) NO_x Emission for Beijing, Aug-2022



(f) NO_x Column concentration for Beijing, Aug-2022



357
358 **Figure 4** Gridded prior NO_x emission inventories derived from the mass balance method. Panels (a)–(c) show the NO_x flux distributions
359 (unit: mol/m²/s) for Beijing, Paris, and Cairo in August 2022. Panels (d)–(f) present the resampled monthly mean NO₂ column

360 concentration distributions for the three cities. Basemap for panels (a)–(c): Esri World Topographic Map. Sources: Esri, HERE, Garmin,
361 Intermap, INCREMENT P, GEBCO, USGS, FAO, NPS, NRCan, GeoBase, IGN, Kadaster NL, Ordnance Survey, Esri Japan, METI,
362 Mapwithyou, NOSTRA, © OpenStreetMap contributors, and the GIS user community.

363
364 To quantitatively compare the NO_x emission characteristics and atmospheric behavior among Beijing, Paris, and Cairo, derived
365 using the mass balance approach, we analyzed key parameters for August, including mean NO_x fluxes, total emissions, chemical
366 lifetimes, vertical distribution scale heights, and NO_x/NO₂ ratios (Table 1). These NO_x behavior parameters reflect heterogeneous
367 characteristics shaped by the interplay of emission intensity, photochemical conditions, and boundary layer structure.

368 In terms of mean NO_x flux per unit area ($\text{mol m}^{-2} \text{s}^{-1}$), Cairo exhibits the highest value (0.35×10^{-8}), followed by Paris ($0.28 \times$
369 10^{-8}) and Beijing (0.24×10^{-8}), indicating a higher emission of urban emission sources in Cairo—particularly from traffic—resulting
370 in stronger NO_x release per unit surface area. Nevertheless, Beijing’s total NO_x emissions ($182,800 \text{ t yr}^{-1}$) are substantially higher
371 than those of the other two cities, reflecting its larger urban extent and greater overall emission intensity, characteristic of a complex
372 multi-source emission profile.

373 The first-order chemical lifetime of NO_x in the atmosphere indicates its removal rate and is influenced by factors such as OH
374 radical concentration and solar radiation intensity. Paris exhibits the longest NO_x chemical lifetime (6.91 h), followed by Beijing
375 (4.70 h) and Cairo (2.93 h). These differences are closely linked to photochemical activity: strong summer sunlight and high
376 temperatures in Cairo enhance OH-driven removal reactions, whereas the relatively mild mid-latitude climate of Paris, combined
377 with emission control measures, prolongs NO_x lifetime.

378 Regarding vertical distribution, the NO_x scale height also varies across the three cities. Beijing shows the highest scale height
379 (2.08 km), reflecting the combined effects of strong convective transport and multi-source emissions that elevate NO_x into the upper
380 mixing layer. By contrast, Cairo (1.41 km) and Paris (1.21 km) display more typical boundary-layer-constrained distributions,
381 indicating that ground-level emission controls and thermal structure strongly modulate vertical NO_x transport.

382 Finally, the NO_x/NO₂ ratio provides insight into the proportion of NO and its degree of conversion. Beijing exhibits the highest
383 ratio (1.41), followed by Cairo (1.32) and Paris (1.29), suggesting a higher fraction of NO in Beijing, likely associated with dense
384 traffic sources and a larger fraction of primary NO emissions. The relatively lower ratio in Paris reflects a higher NO₂ fraction,
385 consistent with effective emission controls and extensive photochemical conversion.

386
387 **Table 1 Grid-averaged NO_x fluxes, with total urban NO_x emissions as intermediate parameters in the mass balance method.**

City	NO _x average flux mol/(m ² * s)	NO _x total emission kt/month	Chemical lifetime(hour)	Scale height(km)	NO _x /NO ₂
Beijing	0.235×10^{-8}	15.29	4.69	2.07	1.41

Paris	0.277 10 ⁽⁻⁸⁾	4.45	6.90	1.21	1.29
Cairo	0.353 10 ⁽⁻⁸⁾	6.78	2.93	1.40	1.32

388 **Details of the uncertainties are provided in the Appendix A5.**

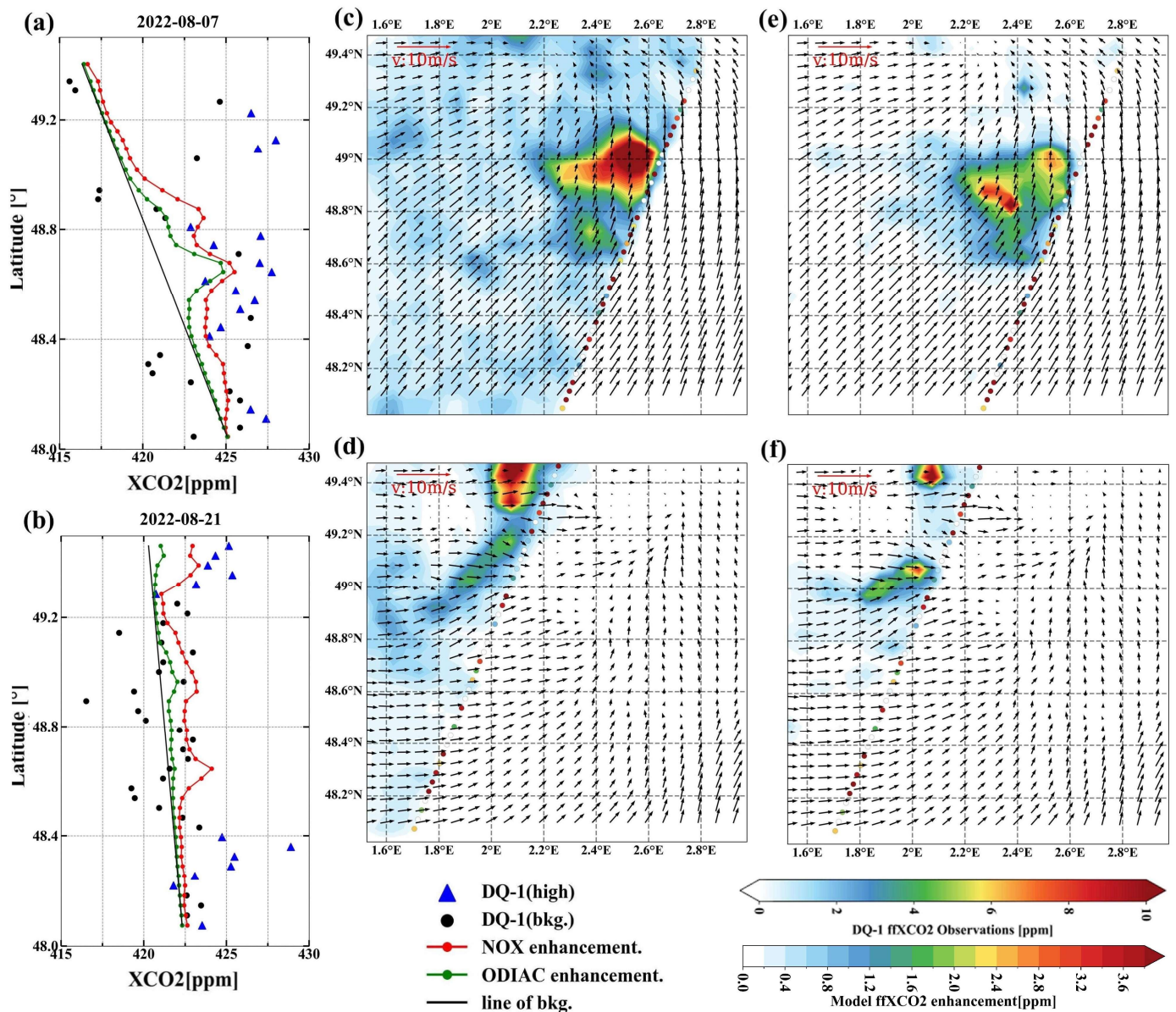
389 **3.2. Urban Fossil Fuel XCO₂ Enhancement (ffXCO₂)**

390 In this section, we summarize the prior ffXCO₂ emissions for each study region. For the selected orbits, the total monthly
391 emissions of Beijing, Paris, and Cairo were approximately 7.47–9.94, 2.91–3.33, and 2.73–3.60 MtC/month, respectively. To
392 constrain emissions, we compared observed and simulated ffXCO₂ enhancements, where ffXCO₂ enhancement is defined as the
393 increase in XCO₂ relative to the background level caused by local fossil fuel emissions. The prior ffXCO₂ enhancements were
394 simulated by taking the inner product of prior NO_x emissions inventories with STILT footprints, while the observed enhancements
395 from DQ-1 were derived by subtracting the background concentration from the measured XCO₂. By comparing prior and observed
396 ffXCO₂ enhancements, we assessed the variability of ffXCO₂ along the orbit and investigated the sources and detectability of the
397 ffXCO₂ signal.

398 **3.2.1. Comparison of Modeled and Observed ffXCO₂**

399 Complex horizontal wind fields can lead to elongated and non-Gaussian plume structures in simulated ffXCO₂ distributions (Ye
400 et al., 2020). This feature is illustrated in Fig. 5c–f. Figures 5a and 5b show the simulated and observed XCO₂ along two overpasses
401 (simulated XCO₂ is obtained by adding the simulated ffXCO₂ to the background derived in Section 2.2.2 (1)). Along these overpasses,
402 ffXCO₂ enhancements exceeding 5 and 10 ppm were observed, with the measured enhancements consistently larger than the
403 simulated values. Although the simulated peak on 7 August is narrower than the observed peak, and the observed peak near 48.4°
404 on 21 August shows a ~0.3° displacement relative to the simulation, the overall magnitude of simulated ffXCO₂ agrees well with
405 observations.

406 To further evaluate the feasibility of constraining fossil fuel CO₂ emissions using the NO_x inventory, we performed a
407 comparative analysis using the ODIAC inventory. We compared simulated ffXCO₂ during the satellite overpasses based on the NO_x
408 and ODIAC inventories (colored shaded areas in the figure), as well as their contributions to the pseudo-observed XCO₂ at the
409 satellite locations (colored dots), where the red line represents enhancements derived from the NO_x inventory and the green line
410 represents those from ODIAC. Over Paris, the NO_x-based simulation yields higher ffXCO₂ enhancements than ODIAC, likely due
411 to uncertainty in the prior CO₂-to-NO_x ratio. Nonetheless, both inventories capture enhancements exceeding 4 ppm. Moreover, the
412 line plots indicate that the temporal variation and magnitude of the simulated concentration contributions (red and green lines) are
413 nearly identical.

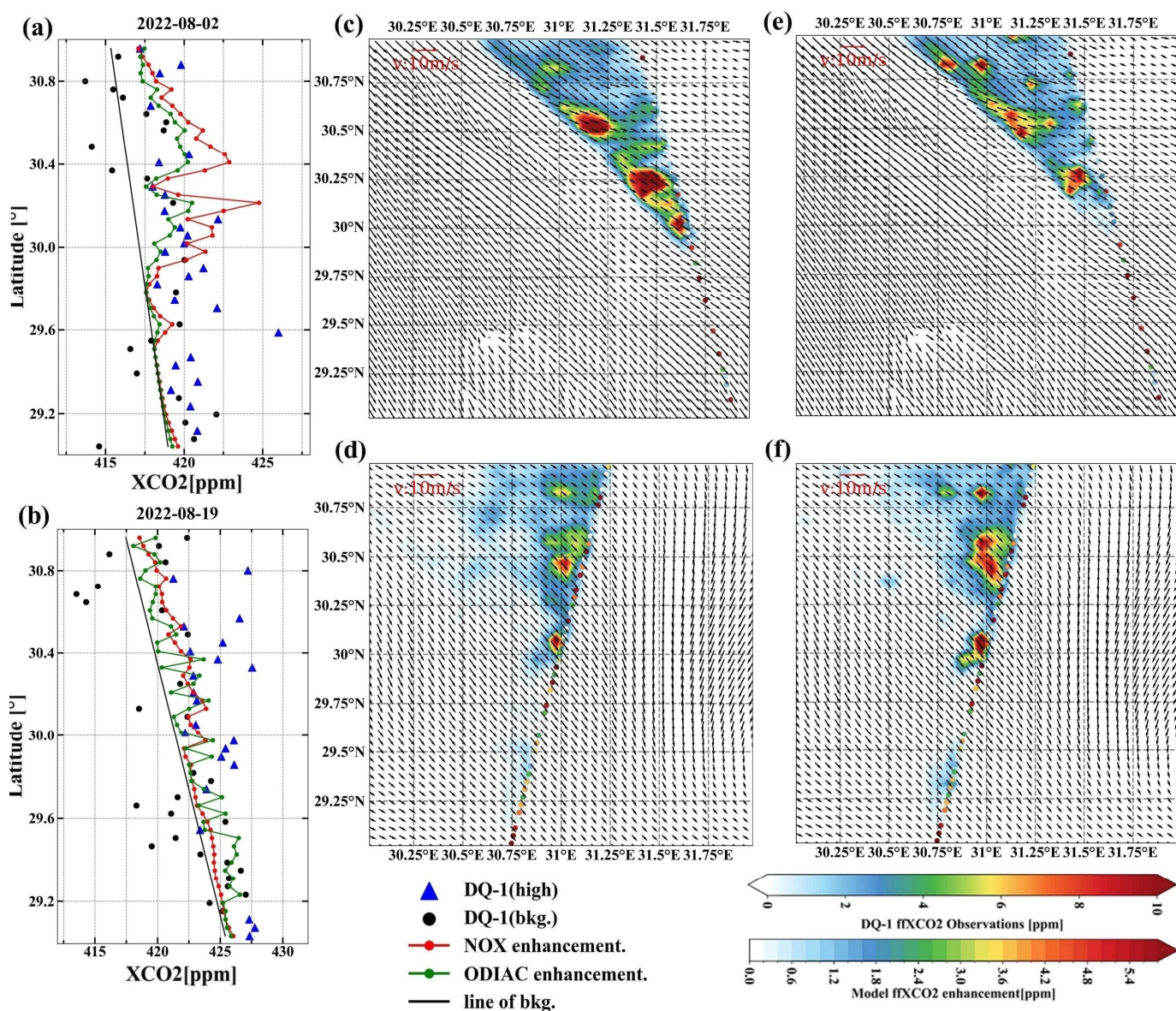


414
 415 **Figure 5 Comparison between simulated and observed fXCO₂ enhancements using DQ-1 overpasses above Paris on 7 August 2022 and**
 416 **21 August 2022 at 01:00 UTC. Panels (a) and (b) show DQ-1 XCO₂ along the two tracks (black dots and blue triangles) and simulated**
 417 **XCO₂ (red solid line: sum of background concentration and fXCO₂ simulated using the NO_x emissions; green solid line: sum of**
 418 **background concentration and fXCO₂ simulated using the ODIAC inventory), averaged over 0.5 s. Black circles denote the data used to**
 419 **derive the background concentration (black solid line). Panels (c)–(f) show simulated fXCO₂ and observed fXCO₂ retrieved from DQ-1**
 420 **data ((c), (d): based on the NO_x inventory; (e), (f): based on the ODIAC inventory). Background XCO₂ concentrations have been subtracted.**
 421 **The reference vector indicates a wind speed of 10 m/s.**

422
 423 We examined local fXCO₂ enhancements during two overpasses of Cairo on 2 August 2022 at 11:00 and 19 August 2022 at
 424 23:00. As shown in Fig. 6, the simulated fXCO₂ peaks exceed 6 ppm. In contrast to Paris, where enhancements are widespread,
 425 diffuse, and lack clear structure, and Beijing, where plumes exhibit complex patterns, the simulated fXCO₂ over Cairo is strongly
 426 influenced by northwesterly winds, resulting in well-defined plumes. Figure 5a illustrates that the simulations based on both
 427 inventories on 2 August produce similar magnitudes and trends, consistent with the Paris results, where the NO_x-based simulation

428 exceeds that from ODIAC. Notably, the simulated peaks on 2 August also show a spatial offset relative to the observations.
 429 Following Ye et al. 2020, such offsets are attributed to the satellite trajectory crossing the plume edges nearly parallel to the plume
 430 axis, making the simulated ffXCO₂ highly sensitive to errors in the horizontal wind field.

431 Notably, the overpasses above Paris and Cairo (Figs. 5a and 6b) exhibit higher latitudinal gradients in the background XCO₂,
 432 as indicated by the background lines. The approach used to derive these background lines provides a reliable estimate of background
 433 XCO₂ because, within the relevant regions, the observed and modeled cumulative ffXCO₂ enhancements along the satellite track
 434 are largely consistent. Consequently, these findings highlight the effectiveness of the background line method for inferring satellite-
 435 observed background XCO₂. They also emphasize that the spatial scale of satellite data analysis is closely linked to the constraints
 436 imposed by local emission sources. Neglecting the latitudinal gradient of background XCO₂ may introduce biases in the estimation
 437 of ffXCO₂ and, consequently, in derived emission fluxes(Ye et al., 2020).

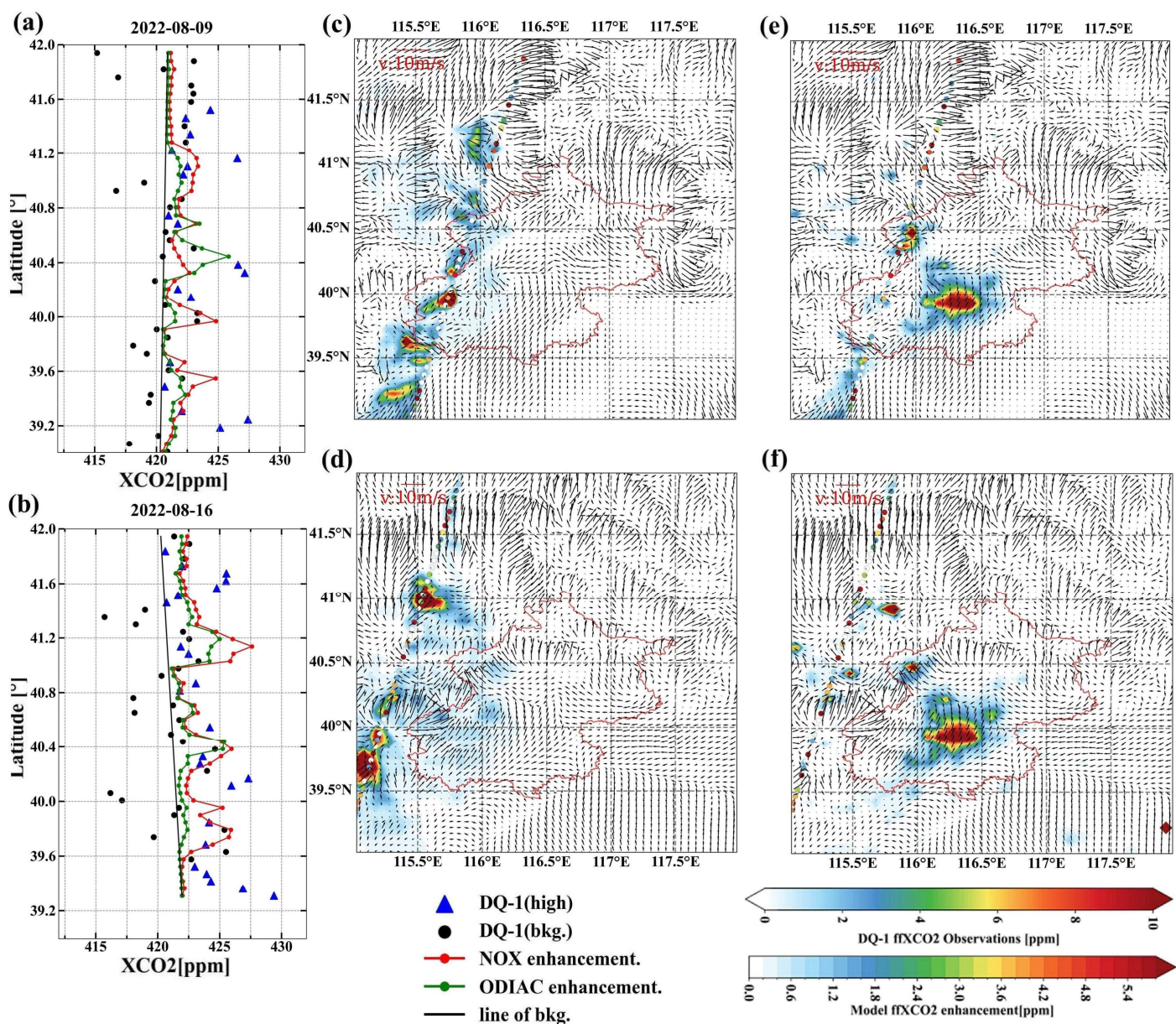


438
 439 **Figure 6** Similar to Fig. 5, comparison between simulated and observed ffXCO₂ enhancements using DQ-1 overpasses above Cairo on 2
 440 August 2022 at 11:00 UTC (panels a, c, e) and 19 August 2022 at 23:00 UTC (panels b, d, f). Panels (c) and (d) show the simulated ffXCO₂

441 enhancements based on the NO_x emissions, while panels (e) and (f) show those based on the ODIAC inventory.

442

443 3.2.2. Comparison of NO_x and ODIAC Modeled ffXCO_2 in Beijing



444

445 Figure 7 Similar to Fig. 5, comparison between simulated and observed ffXCO_2 enhancements using DQ-1 overpasses above Beijing on 9
446 August 2022 at 18:00 UTC (panels a, c, e) and 16 August 2022 at 18:00 UTC (panels b, d, f). Panels (c) and (d) show the simulated ffXCO_2
447 enhancements based on the NO_x emissions, while panels (e) and (f) show those based on the ODIAC inventory.

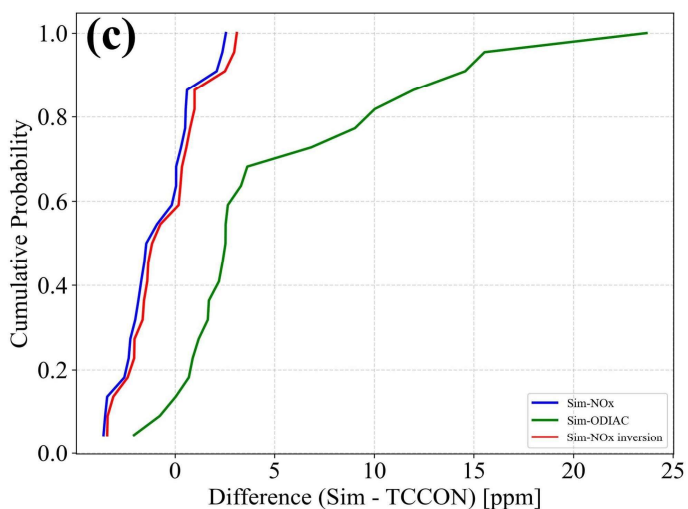
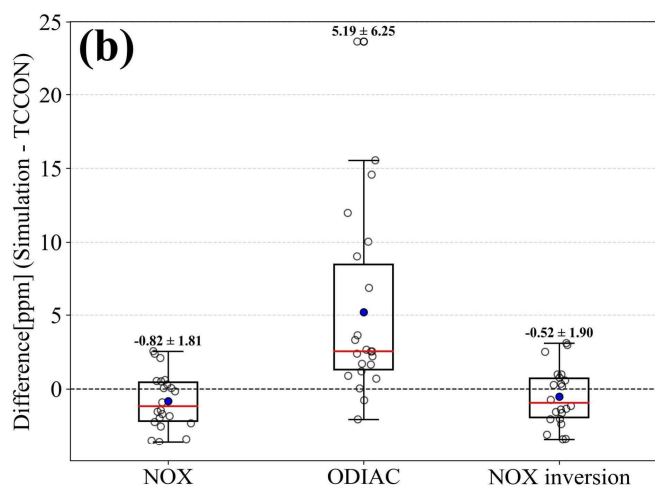
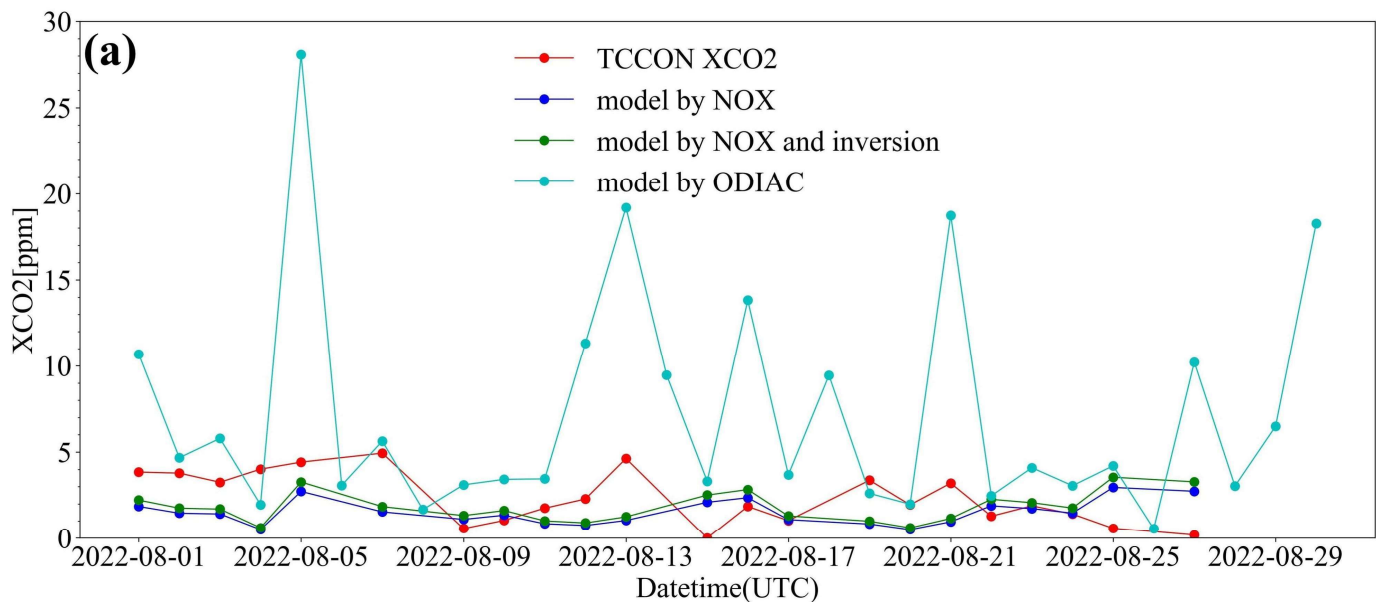
448

449 Figure 7 illustrates the investigation of local ffXCO_2 enhancements over Beijing using two DQ-1 overpasses and corresponding
450 simulated ffXCO_2 . In the figure, the colored shading represents XCO_2 concentrations accumulated over the previous 24 hours
451 simulated by STILT, while the colored dots indicate satellite-observed XCO_2 enhancements, calculated by subtracting the

452 background values (see Section 2.2.2). The red contours outline the urban area of Beijing. As shown, ffXCO₂ over this region can
453 reach approximately 6.0 ppm.

454 Notably, simulations based on the NO_x inventory (Figs. 7c, d) show that the spatial distribution of ffXCO₂ enhancements varies
455 significantly with meteorological conditions and emission patterns. In contrast, for Paris and Cairo, the simulated ffXCO₂ is more
456 concentrated. Over Beijing, however, the ffXCO₂ distribution is more dispersed and comprises multiple plumes. When comparing
457 simulations using NO_x and ODIAC inventories for Paris and Cairo, the overall plume structures remain largely unaffected. Over
458 Beijing, the simulations using the ODIAC inventory (Figs. 7e, f) display an almost identical ffXCO₂ enhancement distribution across
459 different wind conditions, showing pronounced anomalies in the urban area. Such similarity is unrealistic.

460 We attribute this behavior to the ODIAC inventory allocating disproportionately high fossil fuel emissions to central Beijing.
461 When STILT footprints intersect the urban area, the high emission gradients in ODIAC (central urban emissions far exceeding
462 suburban values) amplify ffXCO₂ enhancements in the inner city. ODIAC's low-emission thresholds are influenced by nighttime
463 light saturation, with median differences ranging from 47% to 84%. Consequently, ODIAC artificially concentrates emissions in the
464 city center while underrepresenting surrounding suburban areas. This makes it challenging to accurately constrain CO₂ fluxes in the
465 peripheral regions using ODIAC. Observations from the TCCON Xianghe site further highlight the limitations of ODIAC's emission
466 allocation in the Beijing area.



467
 468 **Figure 8 Comparison of ffXCO₂ observed at the TCCON Xianghe site in Beijing during August with ffXCO₂ simulated using the NO_x**
 469 **inventory and the ODIAC inventory. Panel (a) shows the ffXCO₂ observed by TCCON (red line), simulated ffXCO₂ using the NO_x**
 470 **emissions (dark blue line), simulated ffXCO₂ using the ODIAC inventory (light blue line), and simulated ffXCO₂ using the posterior NO_x**
 471 **emissions (green line). Panel (b) presents the distribution of differences between simulated ffXCO₂ (from the NO_x and ODIAC inventories)**
 472 **and TCCON observations throughout August, with bold numbers indicating the mean and standard deviation. Panel (c) shows the**
 473 **cumulative probability distributions of the differences between simulated ffXCO₂ (NO_x emissions and ODIAC inventory) and TCCON**
 474 **observations.**

475
 476 Figure 8 presents the comparison of August ffXCO₂ at the TCCON site with simulations using the ODIAC and NO_x inventories.
 477 Unlike the ffXCO₂ calculation described in Section 2.2.2, the TCCON observations provide daily-averaged fossil fuel CO₂
 478 enhancements, where TCCON ffXCO₂ is calculated as TCCON XCO₂ minus background XCO₂ and NEE contributions (details in
 479 the Appendix A3). In Figure 8a, the dark blue line represents ffXCO₂ simulated at the TCCON site using the NO_x inventory, the
 480 green line shows the ffXCO₂ simulated after optimization with the inversion using DQ-1 observations, the light blue line corresponds
 481 to ODIAC-based simulations, and the red line depicts TCCON-observed ffXCO₂.

482 Figure 8b quantifies the accuracy of the simulations by plotting the difference between the simulated ffXCO₂ and TCCON
 483 observations on the same day and summarizing the monthly mean and standard deviation. The monthly mean absolute difference
 484 for the NO_x inventory is 0.82 ppm, while ODIAC exhibits a much larger discrepancy of 5.19 ppm. The inversion-constrained NO_x
 485 inventory reduces the mean absolute difference to 0.52 ppm, closely matching TCCON observations. Figure 8c shows the
 486 cumulative probability distribution of the differences between simulated and observed ffXCO₂. The differences for the NO_x and
 487 inversion-constrained NO_x simulations are largely centered around zero (blue and red lines), whereas for ODIAC, approximately
 488 30% of differences exceed 5 ppm.

489 These results indicate that for Beijing in August, simulations based on the NO_x inventory outperform those using ODIAC.
 490 Given that the prior ffCO₂ emissions in both inventories are of similar magnitude, the observed discrepancies are primarily
 491 attributable to the spatial allocation of emissions in ODIAC. The combined inversion using TROPOMI and ACDL data provides a
 492 more accurate reconstruction of urban ffXCO₂ plume structures.

493 3.2.3. ffCO₂ Inversion Results

494 **Table 2 Results of inversion of for CO₂-to-NO_x ratio selected cities using DQ-1 XCO₂ data**

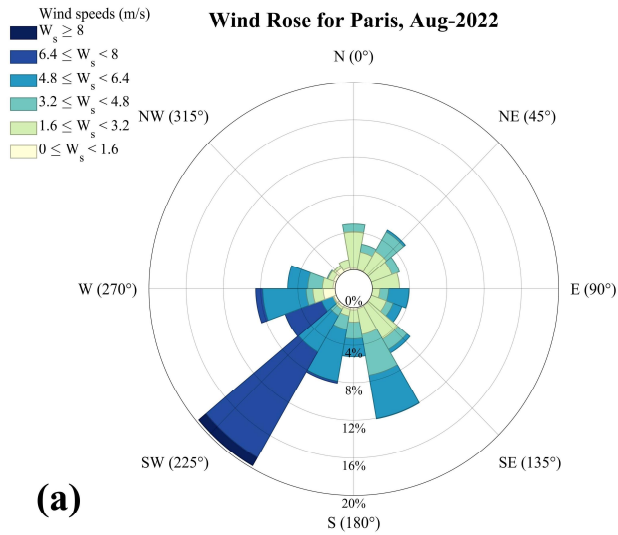
City	Overpass	Prior CO ₂ -to- NO _x ratio (λ)	Prior uncertainty (%)	Observation uncertainty (ppm)	Model transport uncertainty (ppm)	Posterior CO ₂ -to-NO _x ratio (λ) and uncertainty
Cairo	2022/08/02	470	40.59%	1.23	1.75	428±64.58
	2022/08/19			1.06	2.10	512±96.56
Paris	2022/08/07	601	30.12%	2.45	0.36	731±107.60
	2022/08/21			1.68	0.76	742±138.53
Beijing	2022/08/09	694	28.12%	2.31	1.28	640±90.11
	2022/08/16			1.79	3.25	553±89.80

495 This section presents the inversion results of urban carbon emissions for Cairo, Paris, and Beijing, based on TROPOMI and
 496 DQ-1 satellite overpass observations (see Table 2). In the inversion, we systematically accounted for observational errors and
 497 uncertainties in atmospheric transport to improve the reliability of the emission estimates. From the posterior results, we derived
 498 city-specific CO₂-to-NO_x ratios and, by combining them with TROPOMI-derived NO_x emissions, further quantified fossil fuel CO₂
 499 (ffCO₂) emissions. This approach not only enables quantitative assessment of emissions but also provides a scientific basis for cross-
 500 city comparisons of emission characteristics, while demonstrating the potential of multi-satellite data for urban emission monitoring.

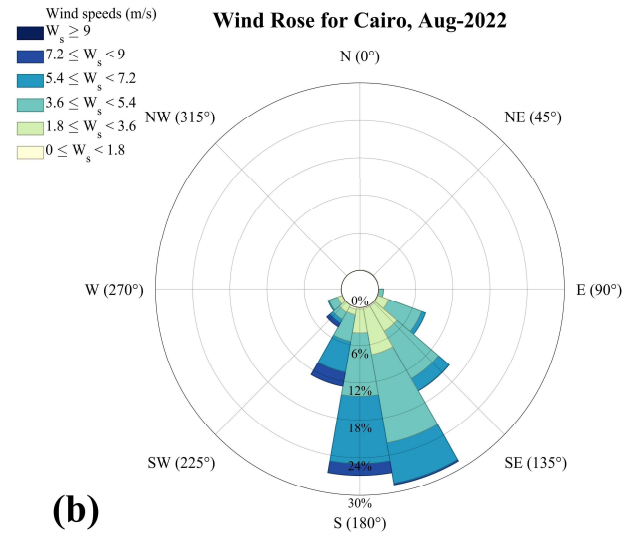
501 For the selected orbits, the posterior CO₂-to-NO_x ratios were 428–512 for Cairo, 731–742 for Paris, and 553–640 for Beijing

(Table 2). These ratios exhibited clear temporal variability under different background conditions. The magnitude of emissions captured by each orbit depended strongly on its distance from major emission regions and the contemporaneous domain-averaged wind conditions (Che et al., 2022). The domain-averaged wind speeds for the study month (Fig. 9), as well as the high-resolution wind fields at overpass time (black arrows in Figs. 5–7), were consistently greater than 3 m s^{-1} . Under such meteorological conditions, the posterior estimates represent emissions from several hours prior to satellite overpass. The posterior uncertainties of the CO_2 -to- NO_x ratio were 15.09%–18.86% for Cairo, 14.72%–18.67% for Paris, and 14.08%–16.24% for Beijing. Overall, uncertainties were larger for Cairo and Paris compared with Beijing.

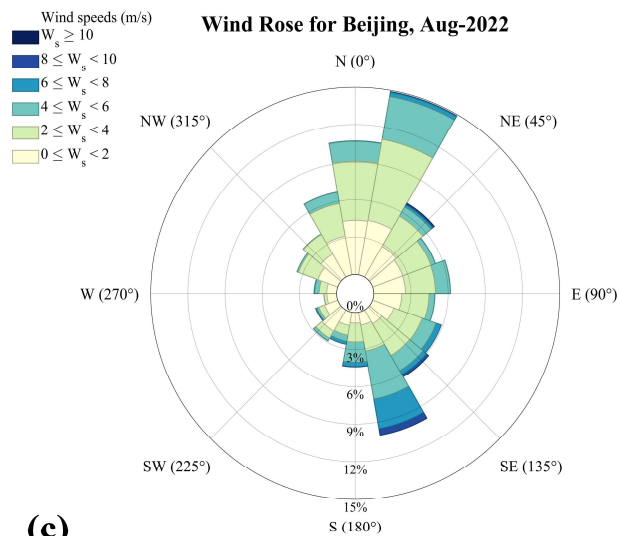
As described in section 4.1, the prior uncertainty of the CO_2 -to- NO_x ratio was prescribed based on available statistics and emission characteristics. Owing to more comprehensive statistics and advanced manufacturing processes, large metropolitan areas typically exhibit better-characterized emission features. Accordingly, the prior uncertainties for Beijing and Paris were smaller than those for Cairo. Table 2 further shows that the relative contributions of observational and transport errors differed across cities. In Cairo, transport errors dominated over observational errors, whereas in Paris the opposite held true. For Beijing, the relative magnitudes of transport and observational errors varied across orbits. The overall smaller posterior uncertainty for Beijing compared to Cairo and Paris reflects its more stable prior emission characteristics.



(a)



(b)



(c)

Figure 9 Monthly mean wind rose plots for Cairo, Paris, and Beijing in August.

3.3. The Uncertainty of Transport Model

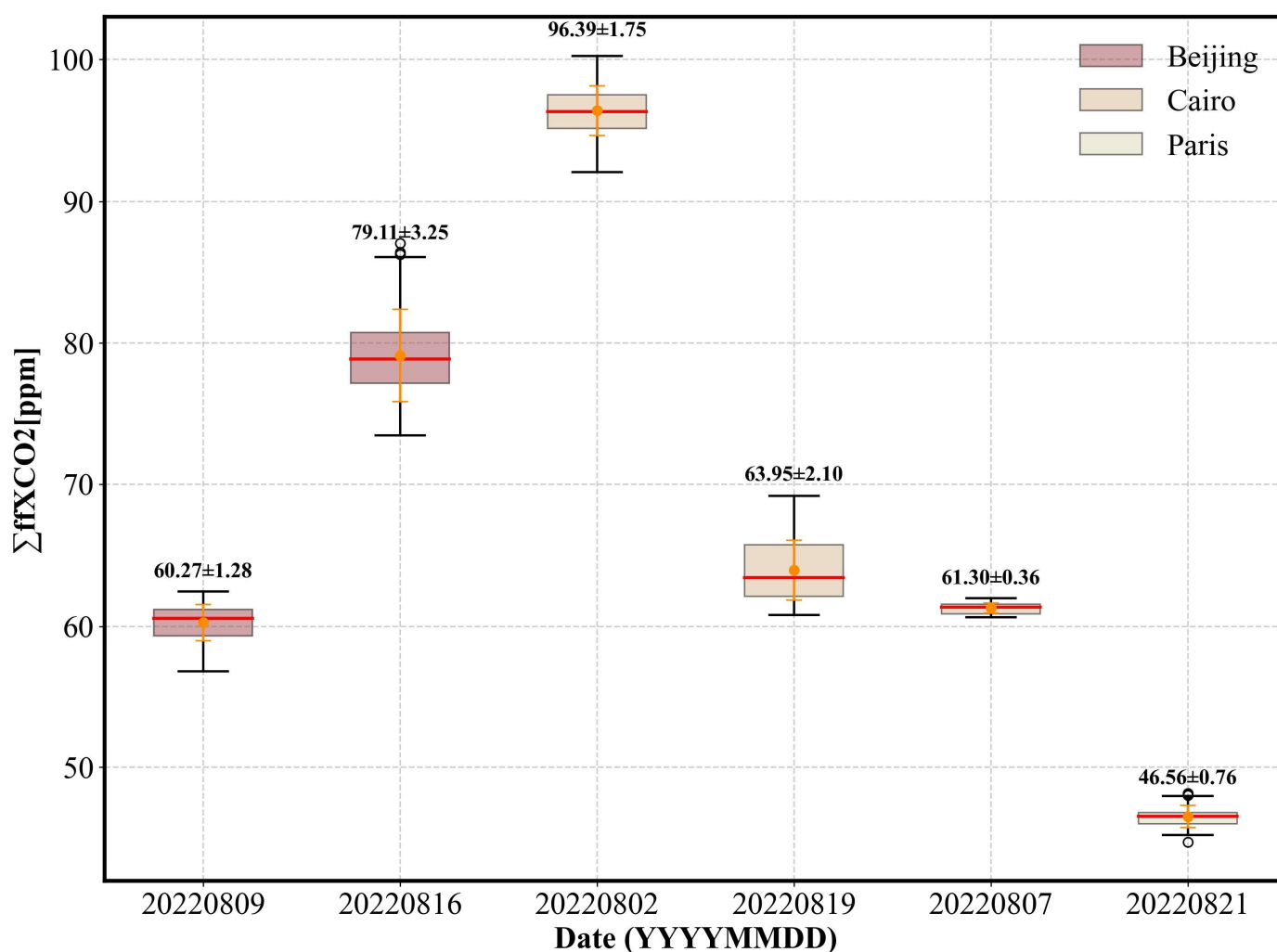
Atmospheric transport modeling uncertainty has been recognized as a major factor affecting emission constraints (Wu et al., 2018). Systematic errors arising from a combination of transport model biases and misrepresented statistical inputs can reduce the magnitude and spatial coverage of terrestrial uncertainty reductions by roughly a factor of two. Notably, transport-related uncertainties in ffXCO_2 represent a key source of error in inverse emission estimates (Ye et al., 2020). In this section, we quantify the impact of transport errors on simulated XCO_2 arising from uncertainties in horizontal wind fields and vertical mixing, with a focus on their influence on the inversion of ffXCO_2 fluxes.

Errors induced by wind field uncertainties propagate through the model and affect the accuracy of CO_2 emission estimates (Sheng et al., 2025). Previous studies have accounted for column transport errors by weighting variance relative to pressure and treating each model level independently (Lin and Gerbig, 2005; Wu et al., 2018). Ye et al. 2020 further quantified ffXCO_2

528 simulation uncertainty by introducing random perturbations in wind speed and direction(Ye et al., 2020). Building on these
529 approaches, we investigate how horizontal wind speed and wind direction errors influence inversion performance.

530 Here, horizontal transport error is propagated through the model via its effect on ffXCO₂ plume dispersion(Luo et al., 2026;
531 Qu et al., 2026). For the selected cities, errors are assumed to be unbiased. Wind direction uncertainty is represented by rotating the
532 plume around the emission center, followed by the addition of random wind speed perturbations to the rotated plume. Using DQ-1
533 wind field data, random errors were added at each model level (wind direction perturbation between -10° and 10°, wind speed
534 perturbation between -1 m/s and 1 m/s), and the STILT footprints were recomputed to obtain plume-averaged footprints with random
535 errors included(Yi et al., 2024).

536 In total, 10⁴ simulations were conducted, with the ffXCO₂ integrated along each satellite track. The standard deviation (1σ) of
537 these simulations is used to represent the uncertainty in simulated ffXCO₂ resulting from horizontal transport errors (Figure 10).



538
539 **Figure 10** Boxplots of modeled integrated ffXCO₂ enhancements ffXCO₂ along selected DQ-1 overpasses for the three cities (distinguished
540 by box color) with dates labeled on the x-axis. For each box, the central line represents the median (q₂), and the bottom and top edges
541 represent the 25th and 75th percentiles (q₁ and q₃), respectively. Whiskers extend to the minimum and maximum values. Numbers
542 indicate the mean ± standard deviation.

543

Figure 10 presents the total simulated ffXCO₂ along DQ-1 overpasses for the different study regions. Overall, the simulated ffXCO₂ totals for the three cities are of comparable magnitude. Notably, compared with Beijing and Cairo, the horizontal transport uncertainty along the two Parisian tracks is the lowest, at 0.36 ppm and 0.76 ppm, respectively. In Cairo, the satellite tracks traverse the edges of emission plumes, making the simulations highly sensitive to wind speed and direction, which results in larger transport model errors. Beijing, with its complex terrain and variable wind fields, exhibits more intricate transport uncertainties relative to the other two cities. These observations indicate that transport model uncertainty is closely related to city-scale emissions, the relative alignment of plumes and satellite tracks, model performance, and local topography. Variations in these factors contribute to temporal changes in posterior emission uncertainties along different tracks.

Vertical turbulent mixing governs the vertical transport of air parcels and controls the dilution of surface emissions within the boundary layer (Vertical mixing in atmospheric tracer transport models: error characterization and propagation). Although column-integrated measurements may be less sensitive to the vertical distribution of tracers than in situ observations, errors in planetary boundary layer (PBL) height can still affect column simulations due to wind shear and its interaction with vertical redistribution of tracers (Planetary boundary layer errors in mesoscale inversions of column-integrated CO₂ measurements). It is worth noting that the ACDL instrument includes an aerosol channel capable of providing extinction coefficient profiles and planetary boundary layer height (PBLH) products (Dai et al., 2024). In this study, PBLH data derived from ACDL retrievals are used in the simulations, helping to mitigate errors arising from inaccurate boundary layer height assumptions. Therefore, boundary layer height errors are not considered in the estimation of ffXCO₂.

4. Importance of Satellite Observations for Optimizing the CO₂-to-NO_x Ratio

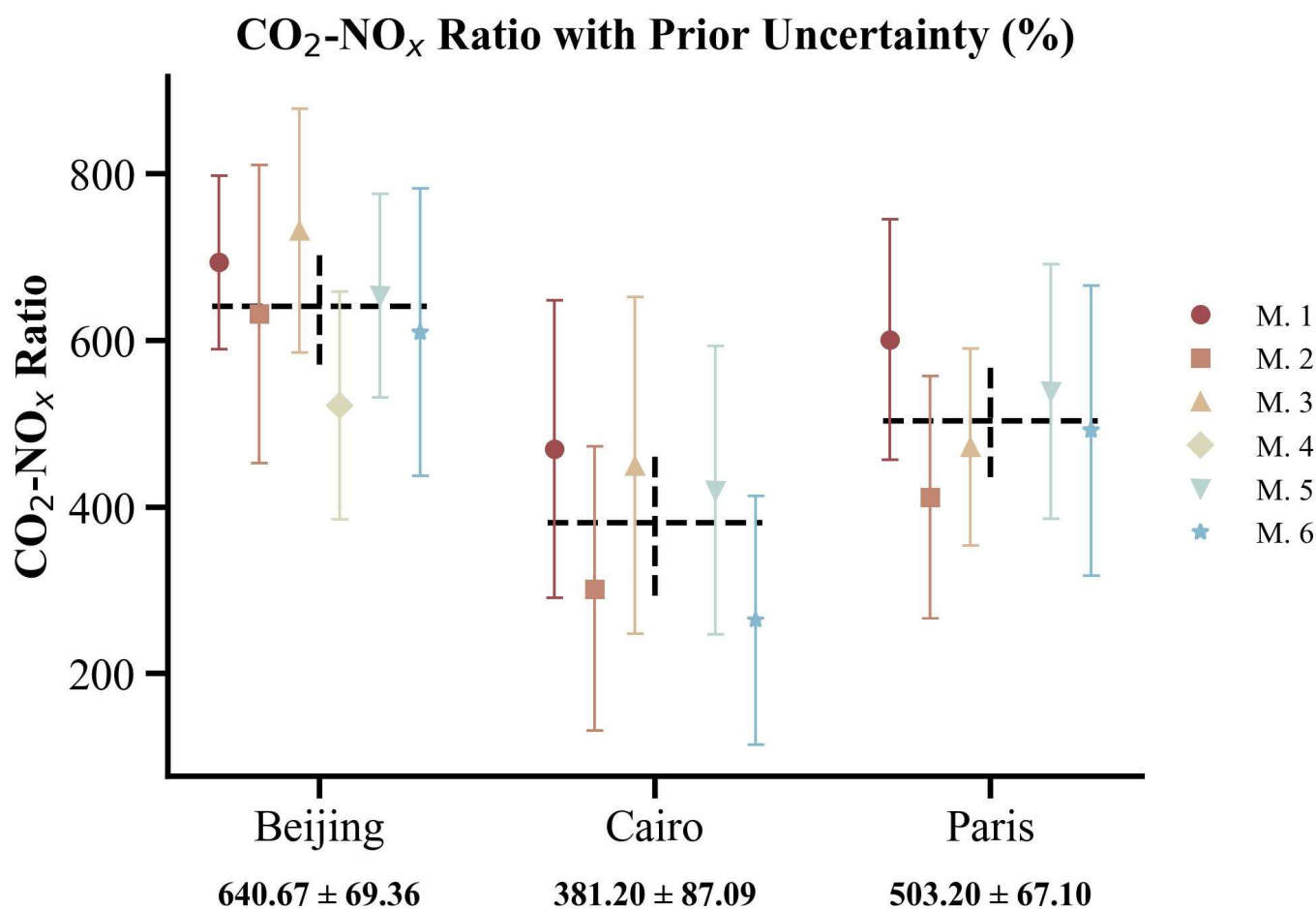
4.1. Variations in CO₂-to-NO_x ratio calculation methods

We systematically accounted for the uncertainties associated with the prior CO₂-to-NO_x ratios for each method (see Section 2.2.1 (4) M1-M6). The uncertainty of the CO₂-to-NO_x ratio arises from the uncertainties of the underlying emissions. For Method 1, a Monte Carlo simulation was performed: CO₂ and NO_x inventory uncertainties (Wang et al., 2013) were used to generate random perturbations at each grid, and the CO₂-to-NO_x ratio was recalculated 10,000 times to obtain the distribution characteristics. The prior CO₂-to-NO_x ratio uncertainty was expressed as R90/M, where R90 is the range between the 95th and 5th percentiles and M is the median value from 10,000 Monte Carlo simulations. For Method 2, the uncertainty was represented as:

$$\sigma_{C/N} = \sqrt{\sigma_{NO_x}^2 + \sigma_{FFCO_2}^2} \quad (14)$$

where σ_{NO_x} and σ_{FFCO_2} denote the uncertainties of the NO_x and ffCO₂ emission factors, respectively. Notably, for each method, the use of different inventories requires adjustment of the assigned uncertainties (see Appendix A6). In Method 3, the prior

572 CO₂-to-NO_x ratio uncertainty was derived from the quadratic sum of observational uncertainties in NO₂ and CO₂ concentrations and
573 the Gaussian fitting uncertainty.



574
575 **Figure 11 Results of CO₂-to-NO_x ratios obtained using different calculation methods for Beijing, Cairo, and Paris. Different CO₂-to-NO_x**
576 **ratios within the same city are distinguished by color. Additionally, the mean and standard deviation of the different ratios for each city**
577 **are also shown.**

578
579 In this section, we used six different CO₂-to-NO_x ratio calculation methods to estimate the city-scale ratios for Beijing, Cairo,
580 and Paris in August. Since the MEIC inventory is only available for Beijing, six prior CO₂-to-NO_x ratios were obtained for Beijing,
581 while five ratios were derived for Paris and Cairo. Figure 11 presents the CO₂-to-NO_x ratios and their associated uncertainties for
582 each city using the different methods. We also calculated the mean and standard deviation of the ratios across methods for each city,
583 reflecting both the overall understanding of the city-scale prior CO₂-to-NO_x ratio and the variability arising from methodological
584 differences.

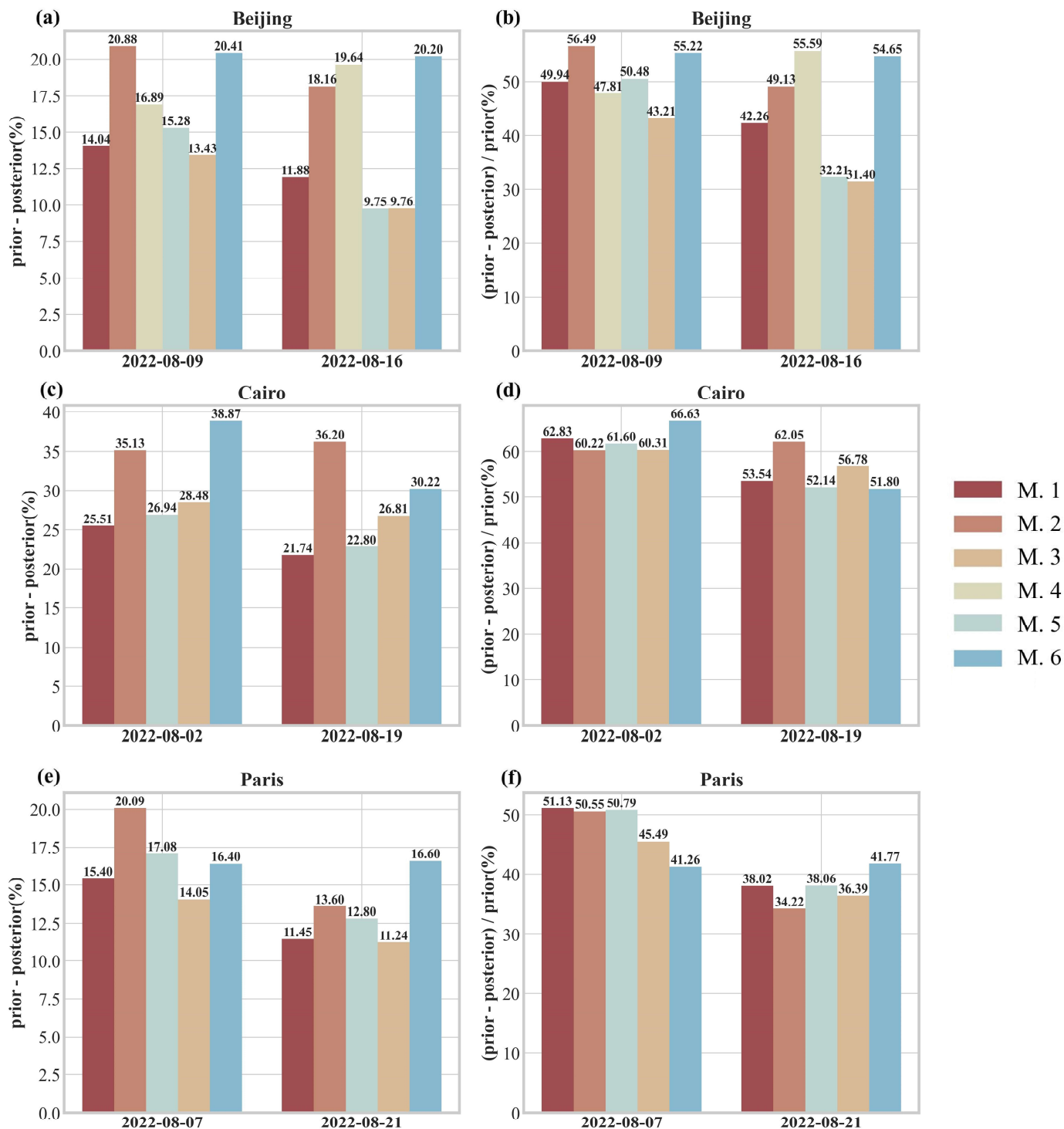
585 The results consistently show the ordering Beijing > Paris > Cairo. Moreover, more developed cities typically have better
586 production technologies and more detailed emission statistics(Oda et al., 2019; Ye et al., 2020). Consequently, the prior uncertainties
587 for Beijing and Paris are notably smaller than those for Cairo, and the variability of CO₂-to-NO_x ratios across methods is also reduced

588 for these cities.

589 **4.2. Bayesian Inversion for Reducing CO₂-to-NO_x Ratio Uncertainty**

590 Using different prior CO₂-to-NO_x ratios, we conducted the Bayesian inversion described in Section 2.2.2 to optimize the August
591 CO₂-to-NO_x ratios for Beijing, Cairo, and Paris along the respective DQ-1 satellite overpasses. Figure 12 shows the absolute
592 reduction in posterior uncertainty (posterior minus prior) and the relative reduction (prior minus posterior, divided by prior) for each
593 city across different orbits. For Beijing, the posterior uncertainty decreased by 9.75%–20.88%, corresponding to a 31.4%–56.49%
594 reduction relative to the prior. In Cairo, the posterior uncertainty decreased by 21.74%–38.87%, equivalent to a 51.8%–66.63%
595 reduction, while in Paris the reduction ranged from 11.24% to 20.09%, corresponding to a 34.22%–51.13% decrease relative to the
596 prior.

597 These results indicate that, for all cities, the posterior uncertainties were significantly reduced regardless of the method used to
598 calculate the prior ratio. This demonstrates that constraining the inversion with DQ-1 ACDL observations substantially improves
599 the accuracy of ffCO₂ estimates derived from NO_x emissions. Notably, in Cairo—the city with the largest prior uncertainty—the
600 reduction in uncertainty after constraining with both active and passive satellite observations was the greatest, highlighting the
601 effectiveness of satellite data in mitigating emission uncertainties in cities with incomplete statistical information. These findings
602 underscore the potential of satellite remote sensing to supplement emission inventories and enhance the reliability of urban emission
603 estimates.

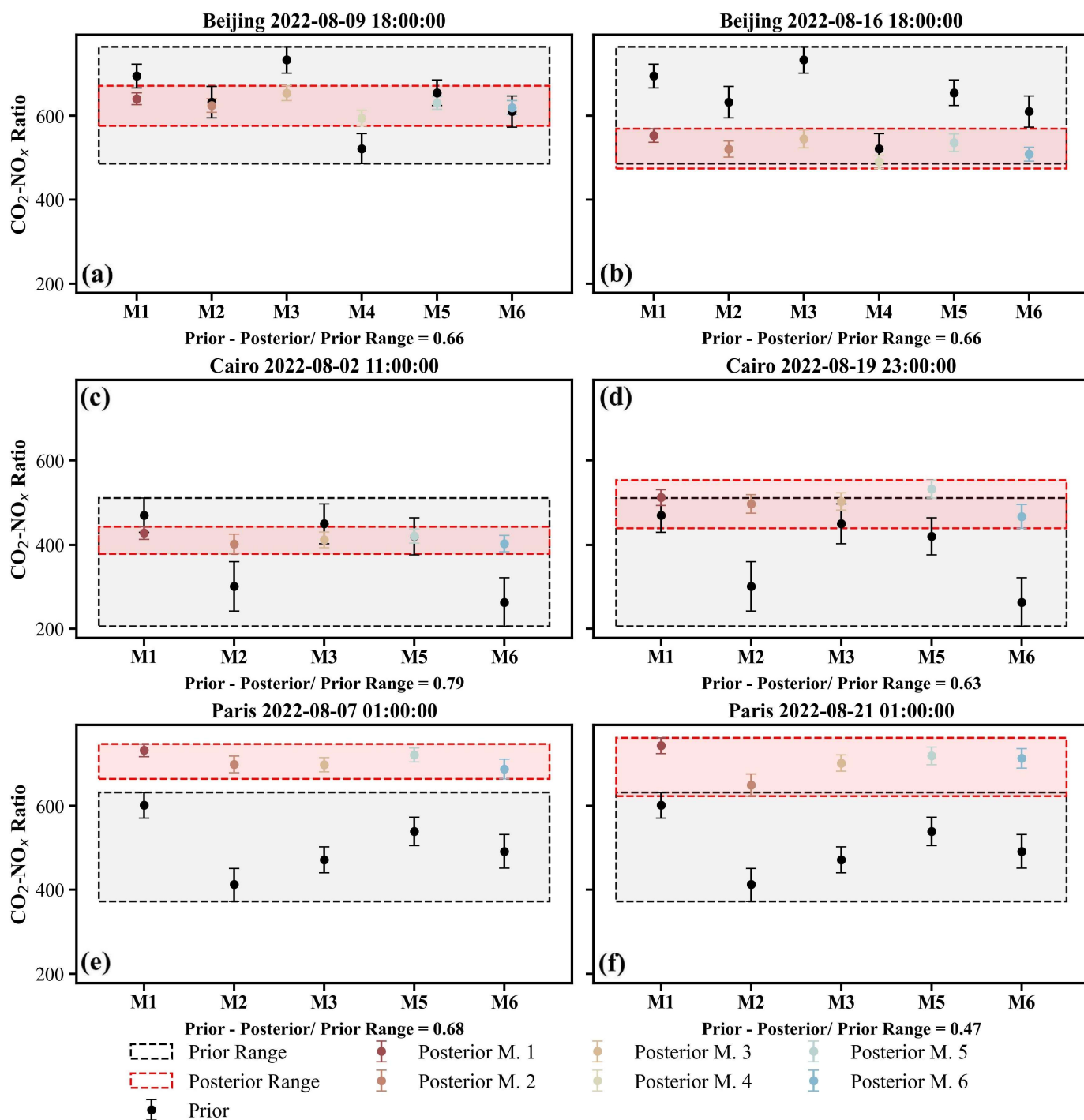


604
 605 **Figure 12 Comparison of Bayesian inversion prior and posterior uncertainties for each orbit over different cities. Panels (a), (c), and (e)**
 606 **show the absolute reduction in uncertainty (prior uncertainty minus posterior uncertainty), while panels (b), (d), and (f) show the relative**
 607 **reduction in uncertainty (prior minus posterior uncertainty divided by prior uncertainty). Results from different prior CO₂-to-NO_x ratios**
 608 **are represented by bars in different colors, with the values displayed at the top of each bar.**

609
 610 Furthermore, we examined the range of CO₂-to-NO_x ratios calculated for each city using different methods (Fig. 13). In the
 611 figure, the black boxes represent the prior distribution ranges, while the red boxes indicate the posterior distribution ranges. The
 612 distribution ranges illustrate the variability among CO₂-to-NO_x ratios obtained from different methods, and we also quantified the

613 reduction of the posterior range relative to the prior. Except for the orbit over Paris on 21 August, all other results show that the
 614 posterior ranges were reduced by more than 60% compared to the priors.

615 These results demonstrate that our approach effectively reduces the discrepancies arising from different CO₂-to-NO_x ratio
 616 calculation methods. That is, prior ratios derived from various methods are constrained to approximately the same range after
 617 inversion. This finding underscores the importance of using observational constraints to obtain more accurate CO₂-to-NO_x ratios in
 618 future ffCO₂ emission estimations.



619
 620 **Figure 13** Distribution ranges of prior and posterior CO₂-to-NO_x ratios calculated using different methods. Black boxes represent the
 621 range of prior CO₂-to-NO_x ratios, with posterior ratios indicated by black circles. Red boxes represent the range of posterior CO₂-to-NO_x

ratios, with posterior uncertainties from different methods shown using different colors and symbols.

5. Summary

Accurate identification and quantification of anthropogenic CO₂ emissions form a critical scientific basis for national emission reduction policies and carbon sink strategies. However, bottom-up inventory approaches typically operate on long compilation cycles (e.g., annual), making it difficult to capture short-term or near-real-time emission dynamics. Most inventories provide only annual totals and lack the temporal resolution needed to characterize daily, hourly, or event-driven emissions.

In this study, we developed a city-scale ffCO₂ inversion framework that integrates both active and passive satellite observations of greenhouse gases. This framework enables high-resolution estimation of fossil fuel emissions at satellite overpass times and over preceding hours, while simultaneously constraining the city-scale CO₂-to-NO_x ratio. A key feature of the approach is its reduced reliance on prior emission inventories, allowing rapid and objective identification and quantification of anthropogenic emission signals at regional scales, thereby enhancing the monitoring and verification of urban emission dynamics. In this framework, satellite-observed XCO₂ enhancements attributed to urban emissions are used to constrain WRF-STILT atmospheric transport simulations of anthropogenic CO₂. This process not only enables quantitative assessment of urban fossil fuel emissions but also provides independent evidence for improving emission inventories and refining urban carbon accounting systems. The study highlights the potential of combining multi-source satellite observations with transport models and lays a foundation for future city-scale ffCO₂ inversions based on the CO₂-to-NO_x ratio. Furthermore, we discuss the impact of the lack of standardized CO₂-to-NO_x ratio calculation methods on urban emission estimates and demonstrate that observational constraints on city-scale ratios can substantially improve ffCO₂ estimation from a carbon-nitrogen co-optimization perspective. Using a Bayesian inversion approach, we optimized the CO₂-to-NO_x ratios for Cairo, Paris, and Beijing in August 2022 based on DQ-1 satellite overpasses and estimated the cities' fossil fuel CO₂ emissions using TROPOMI NO₂ data. The resulting CO₂-to-NO_x ratios ranged from 428–512, 731–742, and 553–640 for Cairo, Paris, and Beijing, respectively, indicating significant day-to-day variability in emission estimates. Cairo exhibited the largest posterior uncertainty, primarily due to high prior uncertainty and transport model errors. Differences in posterior uncertainties across orbits were also closely related to meteorological conditions and the relative position of the satellite tracks to urban plumes. We further compared ffXCO₂ enhancement distributions simulated using the ODIAC inventory. Results for Cairo and Paris were broadly consistent with TROPOMI-based simulations, while notable differences emerged for Beijing. TCCON XCO₂ observations were used to interpret these discrepancies. The monthly mean ffXCO₂ enhancement derived from TROPOMI NO₂ data differed from TCCON measurements by less than 1 ppm, whereas the ODIAC-based results deviated by 5.16 ppm. This highlights the need to account for uncertainties arising from inventory allocation and outdated updates when interpreting XCO₂ inversion results. We systematically examined the impact of different prior CO₂-to-NO_x ratio calculation methods on urban ffCO₂ inversions. In our study, methodological differences led to variations of 10.8%–22.8% in prior ratios. Importantly, regardless of the prior ratio

652 or its uncertainty, DQ-1 observations constrained the posterior values to a similar range, substantially reducing discrepancies among
653 different calculation methods. Another limitation concerns the uncertainty of the divergence-derived NO_x emissions. Although
654 monthly averaging reduces random noise, it does not guarantee that daily divergence errors average to zero. Sampling biases related
655 to clouds, aerosols, surface reflectance, and photochemical variability may persist in the monthly mean. Moreover, gradient
656 operations can amplify white noise in the NO₂ column field and generate structured artifacts in the derived fluxes. Therefore, the
657 current uncertainty estimates should be interpreted as lower-bound, first-order uncertainty estimates. Future work should include
658 more explicit noise-filtering and detection-limit analyses, ideally using ensemble perturbations of the original Level-2 NO₂
659 observations and high-resolution chemical transport simulations to better represent NO₂ profile shapes, lifetimes, and NO_x:NO₂
660 conversion factors. {Cifuentes, 2025 #92; Guan, 2026 #95; Wang, 2025 #91; Zhang, 2026 #96}

661 Looking ahead, improving satellite-based city-scale ffCO₂ inversions will require accounting for the spatiotemporal
662 correlations of prior emission errors. Our current framework does not yet incorporate this aspect, which imposes certain limitations
663 on the interpretation and application of the results. Satellite observations are inherently constrained by inversion errors, sampling
664 geometry, and revisit frequency, limiting overpass opportunities. A single prior factor, such as a uniform CO₂-to-NO_x ratio, cannot
665 fully capture the complex spatiotemporal features of emissions. Incorporating prior error correlations can mitigate uncertainties
666 arising from sparse observations and better resolve temporal and spatial variability in urban emissions. Moreover, the number of
667 satellite tracks required to constrain city emissions depends on the desired emission resolution and uncertainty thresholds relevant
668 for policy applications. Lower temporal resolution may suffice for long-term trend analysis, whereas capturing short-term peaks or
669 episodic emissions necessitates higher observation frequency and precision. This consideration aligns with emerging international
670 approaches emphasizing multi-platform, multi-temporal observations, combining polar-orbiting, geostationary satellites, and
671 ground-based monitoring to achieve multidimensional constraints on urban emissions.

672 Overall, our results demonstrate that coupling high-resolution atmospheric transport simulations with a Bayesian inversion
673 framework allows TROPOMI and DQ-1 multi-source observations to effectively constrain urban ffXCO₂ enhancement signals. The
674 approach captures spatial heterogeneity of emissions, particularly in cities with strong emission intensities and well-defined plume
675 structures, providing a robust basis for quantitative analysis. Furthermore, current methods estimating ffCO₂ from NO_x emissions
676 often lack explicit treatment of CO₂-to-NO_x ratio uncertainty, which can significantly influence inversion outcomes. Differences
677 among calculation methods for the same region can be as large as 258–304. Notably, our inversion framework substantially reduces
678 CO₂-to-NO_x ratio uncertainty, providing more stable priors for urban ffCO₂ estimation. Recent studies suggest the need to further
679 optimize CO₂-to-NO_x emission ratios at regional scales to improve ffCO₂ estimates (Feng et al., 2024). Therefore, we recommend
680 that future NO_x-based ffCO₂ inversion studies adopt observational constraints to refine CO₂-to-NO_x ratios, minimizing errors arising
681 from prior ratio uncertainties.

683 **A1: ACDL XCO₂ Data Inversion**

684 Unlike passive satellite XCO₂ products (e.g., OCO-2/3), the DQ-1 XCO₂ product—hereafter referred to as XCO_2^{Lidar} to
 685 distinguish it from passive measurements—is derived from the differential absorption between ACDL’s on-band wavelength (strong
 686 CO₂ absorption) and off-band wavelength (weak CO₂ absorption). Here, “WF(p)” refers to the lidar signal and integrated weighting
 687 function introduced in Section 2.1.1, with “p” representing atmospheric pressure:

$$688 \quad XCO_2^{Lidar} = \frac{2 \cdot \ln \left(\frac{V_{off} \cdot V_{on-0}}{V_{on} \cdot V_{off-0}} \right)}{\int_{p_{surface}}^{p_{toa}} WF(p) dp} \quad (A1)$$

689 Here, V_{on} and V_{off} denote the reflected signal energies at the on-band and off-band wavelengths, respectively, while V_{on-0}
 690 and V_{off-0} correspond to the transmitted signal energies. $p_{surface}$ represents the atmospheric pressure at the sub-satellite point
 691 of the laser, and p_{toa} denotes the pressure at the top of the atmosphere. The denominator in Equation A1 represents the integrated
 692 weighting function (WF(p)), which can be expressed according to (Refaat et al., 2016) as:

$$693 \quad WF(p) = \Delta\sigma_{wf}(\lambda_{on}, \lambda_{off}, p) \cdot N_{dry}(p) \quad (A2)$$

694 Here, $\Delta\sigma_{wf}(\lambda_{on}, \lambda_{off}, p)$ represents the differential absorption cross-section of CO₂ between the on-band λ_{on} and off-band λ_{off}
 695 wavelengths at pressure p. N_{dry} denotes the number of dry air molecules per unit area within the corresponding pressure layer.

697 **Table A1 DQ-1 ACDL operating parameters**

Parameters	Values
Orbit altitude	705km
Lidar footprint diameter	~70m
Horizontal spacing of lidar footprints	~350m
Field of view	<0.2mrad
Telescope diameter	1000nm
Divergence angle after laser beam expansion	<0.1mrad
Repetition frequency	20Hz
Laser pulse width	<50ns
Laser energy	75mJ
Off-line wavelength	1572.085nm

698

699 **A2: Derivation of the Principle of Mass Balance**700 For satellite column observations of specific species such as NO₂, the mass balance equation can be expressed as follows:

$$701 \begin{cases} \frac{\partial V_{NO_2}}{\partial t} + \nabla \cdot \vec{F}_{NO_2} = E_{NO_2} - S \\ \vec{F}_{NO_2} = V_{NO_2} \vec{u}_{100} \\ S \approx \frac{V_{NO_2}}{\tau} \end{cases} \quad (A3)$$

702 Here, V_{NO_2} represents the columnar NO₂ concentration observed by TROPOMI, defined as a scalar function of x and $\nabla =$
 703 $\left(\frac{\partial}{\partial x}, \frac{\partial}{\partial y}\right)$ denotes the gradient operator; $\vec{F}_{NO_2} = (F_x, F_y)^T$ is the horizontal flux, with units of mol·m⁻²·s⁻¹, expressed as a vector
 704 function of x and y and weighted by the wind vector. The 100 m wind field is commonly used to characterize horizontal transport
 705 within the planetary boundary layer (PBL)(Sun, 2022). τ represents the first-order chemical lifetime of NO₂ in seconds.

706 By solving the system of equations in Equation A3 and expanding the horizontal flux divergence using vector calculus, we
 707 obtain the derivation of Equation A4 from Equation A3:

$$708 \begin{cases} \vec{u}_{100} \cdot (\nabla V_{NO_2}) + V_{NO_2} (\nabla \cdot \vec{u}_{100}) = \nabla \cdot \vec{F}_{NO_2} \\ E_{NO_2} = \frac{\partial V_{NO_2}}{\partial t} + \nabla \cdot \vec{F}_{NO_2} + \frac{V_{NO_2}}{\tau} \end{cases} \quad (A4)$$

709 Sun et al. 2022, in their first-principles derivation, introduced a "topographic correction term" to replace the wind divergence
 710 term $V_{NO_2} (\nabla \cdot \vec{u}_{100})$. Beirle et al. 2023 demonstrated that incorporating a topographic correction significantly improves the inversion
 711 of power-plant NO_x emissions based on the divergence method. Koene et al. 2024 carefully compared these two terms in the
 712 derivation of the divergence method, showing that they originate from the continuity equations of the source and non-source terms,
 713 and that numerically, the wind divergence and wind–topography terms are approximately equal in the absence of observational
 714 errors.

715 Despite their numerical equivalence in derivation, the accuracy of reanalyzed wind fields is generally lower than that of surface
 716 elevation data. Therefore, in practical measurements—particularly in complex, fine-scale settings—the wind divergence term alone
 717 may not provide sufficient constraint. Correcting wind divergence artifacts using topographic gradients is more feasible, especially
 718 in regions with rugged terrain. Accordingly, we revise Equation A5 using Equation A4 as follows:

$$719 \frac{V_{NO_2} \vec{u}_{10} \cdot (\nabla z_0)}{H} \approx V_{NO_2} (\nabla \cdot \vec{u}_{100}) \quad (A5)$$

720 Here, $\frac{V_{NO_2} \vec{u}_{10} \cdot (\nabla z_0)}{H}$ represents the topographic correction term, where the 10 m wind is approximated as the near-surface wind,

and H denotes the gas scale height in meters. Following previous studies (Beirle et al., 2023; Sun, 2022; Liu et al., 2021), Equation A5 is assimilated over both temporal and spatial dimensions. This procedure is concisely represented using the operator $\langle f \rangle$, as introduced in the derivations by Liu et al. and Sun et al. Ultimately, this approach allows the derivation of the vertical NO_2 flux on a grid-resolved basis.

A3: Atmospheric Model Setting

In this study's application of STILT, hourly outputs from version 4.0 of WRF are used to provide high resolution meteorological fields, with the model grid configured to 32 vertical (η) layers. The 6-hourly NCEP FNL (Final) global operational analysis data (ds083.3 , $0.25^\circ \times 0.25^\circ$) are used as initial and boundary conditions for meteorological and land surface fields to provide the initial and boundary conditions for WRF runs. The simulations run for 30 hours, but only the 7th to 30th hours of each simulation are used to avoid spin-up effects in the first 6 hours.

In this study, we used the STILT model, version 2, to simulate atmospheric transport processes. STILT is configured to release 500 particles per receptor each time, with forward dispersion over 24 hours. The particle release heights for STILT are set within the range of 50-1000 m, with releases every 50 m, and 1000-2000 m, with releases every 100 m, the spatial resolution of the STILT simulations is $1 \text{ km} \times 1 \text{ km}$. Generally, as MAXAGL increases from 1 km to 2 km, the urban enhancement increases and then stabilizes.

Table A2 Model version information used in this study

Model	Version
STILT(Stochastic Time-Inverted Lagrangian Transport)	V2
WRF(Weather Research and Forecasting)	V4.0
X-STILT(X-Stochastic Time-Inverted Lagrangian Transport model)	V1

A4: Calculation of NEE XCO_2 enhancement

We performed vertical integration following the method provided by the TCCON team, using the 51 altitude levels listed in the publicly available ak_altitude dataset, which also serve as input heights for the STILT model. In contrast to the XSTILT calculation method used for DQ-1, we applied the integration operator $\text{integration_operator_x2019}$ together with the mean averaging kernel ak_xco2 to the STILT footprints across the 51 levels in order to generate the simulated XSTILT values required for this study. We selected the National Institute for Environmental Studies (Japan) data-driven Upscale Product of Global Gross Primary Production (NEE) as the reference for the overall local NEE during the DQ-1 overpasses. By convolving the NEE inventory with

745 XSTILT, we simulated the XCO₂ enhancement at TCCON sites attributable to NEE.

746 **A5: Calculation of Prior NO_x Emission Uncertainty**

747 The uncertainty estimated here should be regarded as a first-order propagated uncertainty rather than the full uncertainty of the
748 divergence-derived NO_x emissions. In particular, this formulation does not fully capture structured errors arising from finite-
749 difference gradient operators, oversampling from Level-2 observations to Level-3 grids, non-Gaussian retrieval noise, or sampling
750 biases caused by clouds, aerosols, surface reflectance, and photochemical variability. The uncertainty of the NO_x inventory derived
751 from the mass balance approach can be estimated using the error propagation law as follows:

$$752 \quad \varepsilon_{NOx} = \sqrt{\varepsilon_{\alpha}^2 + \varepsilon_{NO2}^2} \quad (A6)$$

753 where ε_{α} represents the uncertainty in the NO_x/NO₂ ratio, its uncertainty arises from the uncertainties in the input parameters
754 of the chemical model(Liu et al., 2022). And ε_{NO2} denotes the uncertainty in the NO₂ flux field. The latter can be further
755 decomposed as:

$$756 \quad \varepsilon_{NO2} = \sqrt{\varepsilon_{TROPOMI}^2 + \varepsilon_{Wind}^2 + \varepsilon_{Fit}^2} \quad (A7)$$

757 Here, $\varepsilon_{TROPOMI}$ is the uncertainty of the NO₂ column concentration, ε_{Wind} represents the uncertainty associated with the wind
758 field, and ε_{Fit} accounts for the uncertainty in the fitted vertical scale height and chemical lifetime. The uncertainty of NO₂ arises
759 from multiple factors, including spectral fitting, stratospheric correction, AMF, clouds, vertical profiles, and surface albedo(Boersma
760 et al., 2018; Verhoelst et al., 2021; Van Geffen et al., 2022; Lu et al., 2025). In this study, we use the ratio of the standard deviation
761 to the mean of the column concentration within the study area as a proxy for the TROPOMI observational noise, integrated over the
762 time series. It should be noted that this proxy is calculated based on the oversampled gridded data (also referred to as Level-3) rather
763 than the original Level-2 orbit data. In this study, we do not account for errors introduced during the oversampling of TROPOMI
764 L2 data to the grid(Glissenaar et al., 2025). With appropriate gridding, the uncertainty in polluted areas can be reduced by
765 approximately 20% compared with the original orbits(Sun et al., 2018a). Wind field uncertainty is quantified through 10⁴ Monte
766 Carlo perturbations of wind speed and direction, with the propagated standard deviation representing the flux variability. The fitting
767 uncertainty is obtained by performing 10⁴ Monte Carlo draws of the grids involved in the fit, generating ensembles of scale heights
768 and chemical lifetimes, with the final fitting error defined as the root mean square of the standard deviations of these ensembles.

769 Using the method described above, we quantified the overall uncertainty of NO_x prior emissions for three cities, as well as the
770 contributions from individual components, with the detailed results summarized in Table A3. It should be noted that the uncertainties
771 reported here represent aggregated values for the entire urban area, rather than detailed uncertainties for individual grid cells.

772 Based on the uncertainty calculations, the total uncertainty is on the order of ~24% for Beijing, ~18% for Paris, and ~14% for

Cairo. A closer look at the contributions of individual components reveals that NO₂ column concentrations and the wind field are the dominant sources, together accounting for more than 66.7% of the total uncertainty. This is attributable to the nature of data-driven dispersion models, in which uncertainties in wind and concentration directly govern the overall uncertainty (Sun, 2022). The nonlinear gradient operations in dispersion models (e.g., second-order difference operators) can amplify white noise in the original concentration field, while in existing emission quantification models, wind fields are considered a major source of uncertainty due to sparse monitoring sites and model errors (Huang et al., 2025).

Among the three cities, NO₂ column inversion uncertainty is highest in Beijing. Unlike Cairo, where high surface reflectivity eases retrievals, Beijing is located in the highly polluted North China Plain with elevated AOD, which increases the difficulty of passive column inversion. In addition, Beijing's complex terrain contributes to the highest wind field uncertainty (~17%) among the three cities. The NO_x/NO₂ uncertainty is roughly similar across the three cities, consistent with previous studies using NU-WRF (~1.4 ± 0.1). In contrast, the uncertainty associated with first-order chemical lifetime and vertical scale height is the lowest among all components (~1%). This is different from earlier studies (~15%) (Liu et al., 2022) and reflects the benefit of the data-driven fitting approach proposed by Sun et al. (see main text). Since no new assumptions were introduced in the current study, this uncertainty arises solely from the linear fitting model.

Table A3 The overall uncertainty of NO_x emissions and the uncertainties of individual components were derived using the dispersion model.

	NO _x /NO ₂ uncertainty(%)	NO ₂ uncertainty(%)	Wind uncertainty(%)	Fitted uncertainty(%)	Total uncertainty(%)
Beijing	6.51	15.49	16.76	1.67	23.79
Cairo	4.79	11.64	6.76	0.78	14.31
Paris	5.02	13.67	10.76	1.21	18.15

A6: Optimization results of the CO₂-to-NO_x ratio obtained using different calculation methods

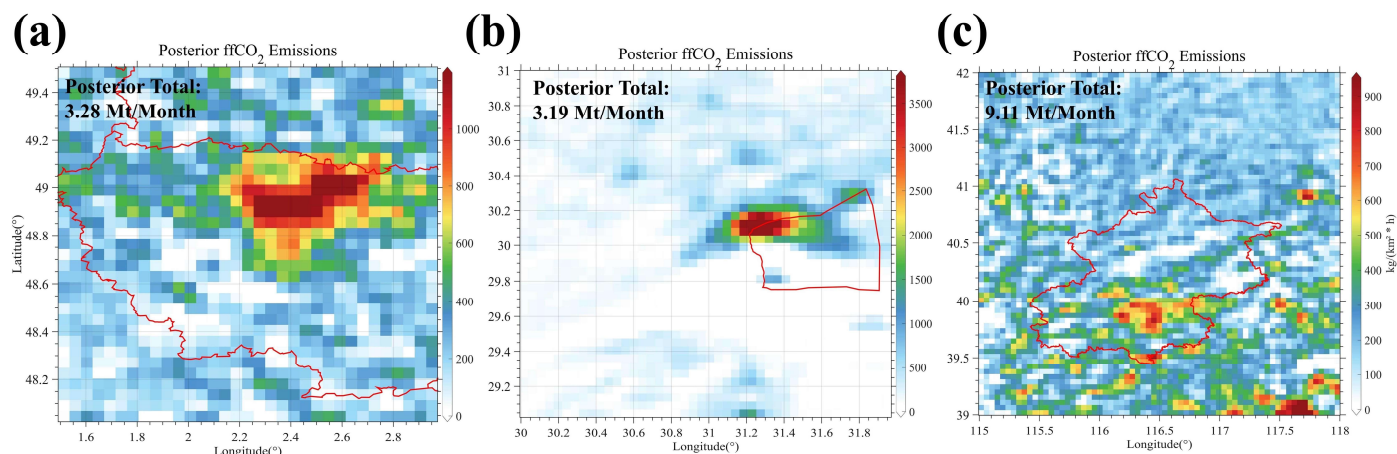
Table A4 Inversion results of CO₂-to-NO_x ratios calculated using different methods

Method	City	Date	Prior CO ₂ - to- NO _x	CO ₂ -to- NO _x ratio uncertainty (%)	NO _x emission uncertainty (%)	Prior uncertainty (%)	Posterior CO ₂ - to-NO _x ratio (λ)	Posterior uncertainty (%)
--------	------	------	--	---	--	-----------------------------	--	------------------------------

			ratio					
			(λ)					
1	Beijing	2022/8/9	694	15	23.79	28.12	640	14.08
	Beijing	2022/8/16	694	15	23.79	28.12	553	16.24
	Cairo	2022/8/2	470	37.99	14.31	40.60	428	15.09
	Cairo	2022/8/19	470	37.99	14.31	40.60	512	18.86
	Paris	2022/8/7	601	24.04	18.15	30.12	731	14.72
	Paris	2022/8/21	601	24.04	18.15	30.12	742	18.67
2	Beijing	2022/8/9	632	28.28	23.79	36.96	624	16.08
	Beijing	2022/8/16	632	28.28	23.79	36.96	521	18.8
	Cairo	2022/8/2	302	56.56	14.31	58.34	402	23.21
	Cairo	2022/8/19	302	56.56	14.31	58.34	497	22.14
	Paris	2022/8/7	412	35.35	18.15	39.74	698	19.65
	Paris	2022/8/21	412	35.35	18.15	39.74	649	26.14
3	Beijing	2022/8/9	732	20.02	23.79	31.09	653	17.65
	Beijing	2022/8/16	732	20.02	23.79	31.09	545	21.32
	Cairo	2022/8/2	450	45.81	14.31	47.99	412	18.74
	Cairo	2022/8/19	450	45.08	14.31	47.99	503	20.41
	Paris	2022/8/7	472	24.83	18.15	30.75	697	16.84
	Paris	2022/8/21	472	24.83	18.15	30.75	701	19.65
4	Beijing	2022/8/9	522	26.12	23.79	35.33	594	18.44
	Beijing	2022/8/16	522	26.12	23.79	35.33	491	15.69
5	Beijing	2022/8/9	654	18.72	23.79	30.27	630	14.99
	Beijing	2022/8/16	654	18.72	23.79	30.27	536	20.52
	Cairo	2022/8/2	420	41.32	14.31	43.73	421	16.79
	Cairo	2022/8/19	420	41.32	14.31	43.73	532	20.93
	Paris	2022/8/7	539	28.31	18.15	33.63	720	16.55
	Paris	2022/8/21	539	28.31	18.15	33.63	718	20.83
6	Beijing	2022/8/9	610	28.28	23.79	36.96	619	16.55
	Beijing	2022/8/16	610	28.28	23.79	36.96	509	16.76

Cairo	2022/8/2	264	56.56	14.31	58.34	403	19.47
Cairo	2022/8/19	264	56.56	14.31	58.34	467	28.12
Paris	2022/8/7	492	35.35	18.15	39.74	687	23.34
Paris	2022/8/21	492	35.35	18.15	39.74	712	23.14

792 **A7: Posterior fossil fuel emissions distribution for each city**



793
794 **Figure A1: Posterior fossil fuel carbon dioxide emissions for each city. The red lines outline city boundaries, while the colored shading**
795 **indicates carbon dioxide emission distribution.**

796 **Declaration of Competing Interest**

797 The authors declare that they have no known competing financial interests or personal relationships that could have appeared
798 to influence the work reported in this paper.

799 **Acknowledgments**

800 The authors thank all the financial support for this research. This research was supported by the National Key R&D Program
801 of China (Grant No. 2024YFB3910203), National Natural Science Foundation of China(Grant No. 42475144), and Beijing Natural
802 Science Foundation (Grant No. L211045).

803 **Author contributions**

804 The experiment design was made by GH and JY. The data collection was done by JY, YH, HL, GH. JY completed the design
805 of the overall WRF-STILT model workflow, data collection, and result analysis. The data analysis was done by HZ, YZ, TS. WG
806 and SL provide funding. The paper was written by JY and GH. All authors have reviewed, commented on, and approved the paper.

- 808 Agency, I. E.: World energy outlook, OECD/IEA Paris2009.
- 809 Beirle, S., Borger, C., Jost, A., and Wagner, T.: Improved catalog of NO_x point source emissions (version 2), *Earth system science*
810 *data discussions*, 2023, 1-37, 2023.
- 811 Boersma, K. F., Eskes, H. J., Richter, A., De Smedt, I., Lorente, A., Beirle, S., van Geffen, J. H. G. M., Zara, M., Peters, E., Van
812 Roozendaal, M., Wagner, T., Maasakkers, J. D., van der A, R. J., Nightingale, J., De Rudder, A., Irie, H., Pinardi, G., Lambert,
813 J. C., and Compernelle, S. C.: Improving algorithms and uncertainty estimates for satellite NO₂ retrievals: results from the
814 quality assurance for the essential climate variables (QA4ECV) project, *Atmos. Meas. Tech.*, 11, 6651-6678, 10.5194/amt-11-
815 6651-2018, 2018.
- 816 Brenninkmeijer, C. A. and Cai, D. S.: Earth System Chemistry integrated Modelling (ESCiMo) with the Modular Earth Submodel
817 System (MESSy) version 2.51, *Geoscientific Model Development*, 9, 1153, 2016.
- 818 Che, K., Lauvaux, T., Taquet, N., Stremme, W., Xu, Y., Alberti, C., Lopez, M., García-Reynoso, A., Ciais, P., and Liu, Y.: CO₂
819 emissions estimate from Mexico City using ground-and space-based remote sensing, *Journal of Geophysical Research:*
820 *Atmospheres*, 129, e2024JD041297, 2024.
- 821 Che, K., Cai, Z., Liu, Y., Wu, L., Yang, D., Chen, Y., Meng, X., Zhou, M., Wang, J., Yao, L., and Wang, P.: Lagrangian inversion of
822 anthropogenic CO₂ emissions from Beijing using differential column measurements, *Environmental Research Letters*, 17,
823 075001, 10.1088/1748-9326/ac7477, 2022.
- 824 Cheng, C., Liu, D., Wang, S., Zhang, X., Zhang, L., Chen, W., Liu, J., Wan, X., Chen, W., and Chen, X.: Estimating strong point
825 CO₂ emissions by combining spaceborne IPDA lidar and HSRL, *Remote Sensing of Environment*, 328, 114898, 2025.
- 826 Crippa, M., Guizzardi, D., Muntean, M., Schaaf, E., Dentener, F., Van Aardenne, J. A., Monni, S., Doering, U., Olivier, J. G., and
827 Pagliari, V.: Gridded emissions of air pollutants for the period 1970–2012 within EDGAR v4. 3.2, *Earth Syst. Sci. Data*, 10,
828 1987-2013, 2018.
- 829 Dai, G., Wu, S., Long, W., Liu, J., Xie, Y., Sun, K., Meng, F., Song, X., Huang, Z., and Chen, W.: Aerosol and cloud data processing
830 and optical property retrieval algorithms for the spaceborne ACDL/DQ-1, *Atmospheric Measurement Techniques*, 17, 1879-
831 1890, 2024.
- 832 Danielson, J. J. and Gesch, D. B.: Global multi-resolution terrain elevation data 2010 (GMTED2010), *US Geological Survey*2331-
833 1258, 2011.
- 834 Dickerson, R. R., Stedman, D. H., and Delany, A. C.: Direct measurements of ozone and nitrogen dioxide photolysis rates in the
835 troposphere, *Journal of Geophysical Research: Oceans*, 87, 4933-4946, 1982.
- 836 Eldering, A., Wennberg, P., Crisp, D., Schimel, D., Gunson, M., Chatterjee, A., Liu, J., Schwandner, F., Sun, Y., and O'dell, C.: The
837 Orbiting Carbon Observatory-2 early science investigations of regional carbon dioxide fluxes, *Science*, 358, eaam5745, 2017.
- 838 Eskes, H., van Geffen, J., Sneep, M., Veeffkind, P., Niemeijer, S., and Zehner, C.: S5P Nitrogen Dioxide v02. 03.01 intermediate
839 reprocessing on the S5P-PAL system: Readme file, ESA, 12,
- 840 Feng, S., Jiang, F., Wang, H., Liu, Y., He, W., Wang, H., Shen, Y., Zhang, L., Jia, M., and Ju, W.: China's fossil fuel CO₂ emissions
841 estimated using surface observations of coemitted NO₂, *Environmental Science & Technology*, 58, 8299-8312, 2024.
- 842 Glissenaar, I., Boersma, K. F., Anglou, I., Rijdsdijk, P., Verhoelst, T., Compernelle, S., Pinardi, G., Lambert, J.-C., Van Roozendaal,
843 M., and Eskes, H.: TROPOMI Level 3 tropospheric NO₂ dataset with advanced uncertainty analysis from the ESA CCI+ ECV
844 precursor project, *Earth System Science Data*, 17, 4627-4650, 2025.
- 845 Hakkarainen, J., Ialongo, I., and Tamminen, J.: Direct space-based observations of anthropogenic CO₂ emission areas from OCO-
846 2, *Geophysical Research Letters*, 43, 11,400-411,406, 2016.
- 847 Han, G., Huang, Y., Shi, T., Zhang, H., Li, S., Zhang, H., Chen, W., Liu, J., and Gong, W.: Quantifying CO₂ emissions of power
848 plants with Aerosols and Carbon Dioxide Lidar onboard DQ-1, *Remote Sensing of Environment*, 313, 114368, 2024.
- 849 Han, G., Wang, H., Pei, Z., Mao, H., Ying, J., Li, S., Ma, X., Liu, B., Mao, F., and Gong, W.: Quantifying facility-scale CO₂
850 emissions using spaceborne hyperspectral imageries, *Remote Sensing of Environment*, 342, 115478, 2026.
- 851 Han, G., Zhang, H., Huang, Y., Chen, W., Mao, H., Zhang, X., Ma, X., Li, S., Zhang, H., and Liu, J.: First global XCO₂ observations

852 fromspaceborne lidar: methodology and initial result, *Remote Sensing of Environment*, 330, 114954, 2025.

853 Hersbach, H., Bell, B., Berrisford, P., Biavati, G., Horányi, A., Muñoz Sabater, J., Nicolas, J., Peubey, C., Radu, R., and Rozum, I.:

854 ERA5 hourly data on single levels from 1940 to present, Copernicus climate change service (c3s) climate data store (cds), 10,

855 2023.

856 Huang, T., Zhu, X., Zhong, Q., Yun, X., Meng, W., Li, B., Ma, J., Zeng, E. Y., and Tao, S.: Spatial and temporal trends in global

857 emissions of nitrogen oxides from 1960 to 2014, *Environmental science & technology*, 51, 7992-8000, 2017.

858 Huang, Y., Han, G., Shi, T., Li, S., Mao, H., Nie, Y., and Gong, W.: Fi-scape: a divergence theorem based emission quantification

859 model for air/space-borne imaging spectrometer derived xch4 observations, *IEEE Journal of Selected Topics in Applied Earth*

860 *Observations and Remote Sensing*, 2024.

861 Huang, Y., Han, G., Yi, J., Shi, T., Zhang, Y., Luo, H., Mao, H., Li, S., Mao, F., and Gong, W.: Rapid methane flux estimation

862 combining MethaneSAT and Sentinel-5P observations: A case study of Turkmenistan, *Geophysical Research Letters*, 52,

863 e2025GL119369, 2025.

864 Kiemle, C., Ehret, G., Amediek, A., Fix, A., Quatrevalet, M., and Wirth, M.: Potential of spaceborne lidar measurements of carbon

865 dioxide and methane emissions from strong point sources, *Remote Sensing*, 9, 1137, 2017.

866 Koene, E. F. M., Brunner, D., and Kuhlmann, G.: On the theory of the divergence method for quantifying source emissions from

867 satellite observations, *Journal of Geophysical Research: Atmospheres*, 129, e2023JD039904, 2024.

868 Kononov, I. B., Berezin, E. V., Ciais, P., Broquet, G., Zhuravlev, R. V., and Janssens-Maenhout, G.: Estimation of fossil-fuel CO

869 2 emissions using satellite measurements of " proxy" species, *Atmospheric Chemistry and Physics*, 16, 13509-13540, 2016.

870 Le Quéré, C., Andrew, R. M., Friedlingstein, P., Sitch, S., Hauck, J., Pongratz, J., Pickers, P. A., Korsbakken, J. I., Peters, G. P., and

871 Canadell, J. G.: Global carbon budget 2018, *Earth System Science Data*, 10, 2141-2194, 2018.

872 Li, H., Liu, B., Gong, W., Ma, Y., Jin, S., Wang, W., Fan, R., and Jiang, S.: Influence of clouds on planetary boundary layer height:

873 A comparative study and factors analysis, *Atmospheric Research*, 314, 107784, 2025.

874 Lin, J. and Gerbig, C.: Accounting for the effect of transport errors on tracer inversions, *Geophysical Research Letters*, 32, 2005.

875 Liu, F., Tao, Z., Beirle, S., Joiner, J., Yoshida, Y., Smith, S. J., Knowland, K. E., and Wagner, T.: A new method for inferring city

876 emissions and lifetimes of nitrogen oxides from high-resolution nitrogen dioxide observations: a model study, *Atmospheric*

877 *Chemistry and Physics*, 22, 1333-1349, 2022.

878 Liu, F., Duncan, B. N., Krotkov, N. A., Lamsal, L. N., Beirle, S., Griffin, D., McLinden, C. A., Goldberg, D. L., and Lu, Z.: A

879 methodology to constrain carbon dioxide emissions from coal-fired power plants using satellite observations of co-emitted

880 nitrogen dioxide, *Atmospheric Chemistry and Physics*, 20, 99-116, 2020.

881 Liu, M., Van Der A, R., Van Weele, M., Eskes, H., Lu, X., Veeffkind, P., De Laat, J., Kong, H., Wang, J., and Sun, J.: A new divergence

882 method to quantify methane emissions using observations of Sentinel-5P TROPOMI, *Geophysical Research Letters*, 48,

883 e2021GL094151, 2021.

884 Lu, L., Cohen, J. B., Qin, K., Tiwari, P., Hu, W., Gao, H., and Zheng, B.: New Perspective on Using Observational Uncertainty to

885 Improve Reliability of NOx Emissions Over Northern China, *IEEE Transactions on Geoscience and Remote Sensing*, 63, 1-

886 15, 10.1109/TGRS.2025.3620116, 2025.

887 Luo, B., Yang, J., Shi, S., Gan, R., Wu, Z., Wang, S., Wang, A., Du, L., and Gong, W.: InceptionFormer: A deep learning framework

888 for UAV LiDAR point cloud completion to improve tree parameters estimation in dense forests, *Remote Sensing of*

889 *Environment*, 338, 115348, 2026.

890 Miller, J. B., Tans, P. P., and Gloor, M.: Steps for success of OCO-2, *Nature Geoscience*, 7, 691-691, 2014.

891 Oda, T., Bun, R., Kinakh, V., Topylko, P., Halushchak, M., Marland, G., Lauvaux, T., Jonas, M., Maksyutov, S., and Nahorski, Z.:

892 Errors and uncertainties in a gridded carbon dioxide emissions inventory, *Mitigation and Adaptation Strategies for Global*

893 *Change*, 24, 1007-1050, 2019.

894 Pei, Z., Han, G., Ma, X., Shi, T., and Gong, W.: A method for estimating the background column concentration of CO 2 using the

895 lagrangian approach, *IEEE Transactions on Geoscience and Remote Sensing*, 60, 1-12, 2022.

896 Qin, K., Lu, L., Liu, J., He, Q., Shi, J., Deng, W., Wang, S., and Cohen, J. B.: Model-free daily inversion of NOx emissions using

897 TROPOMI (MCMFE-NOx) and its uncertainty: Declining regulated emissions and growth of new sources, *Remote Sensing*

898 of Environment, 295, 113720, 2023.

899 Qu, C., Wang, W., Wu, Z., Wang, L., Liu, K., Wu, L., and Miao, Z.: Zero-Shot Vision-Language Model for Rapid Damaged Bridge
900 Extraction in Emergency Response: A Case Study of the 2025 Myanmar Earthquake, *IEEE Geoscience and Remote Sensing*
901 *Letters*, 2026.

902 Refaat, T. F., Singh, U. N., Yu, J., Petros, M., Remus, R., and Ismail, S.: Double-pulse 2- μ m integrated path differential absorption
903 lidar airborne validation for atmospheric carbon dioxide measurement, *Applied Optics*, 55, 4232-4246, 2016.

904 Reuter, M., Buchwitz, M., Schneising, O., Krautwurst, S., O'Dell, C. W., Richter, A., Bovensmann, H., and Burrows, J. P.: Towards
905 monitoring localized CO₂ emissions from space: co-located regional CO₂ and NO₂ enhancements observed by the OCO-2
906 and S5P satellites, *Atmospheric Chemistry and Physics*, 19, 9371-9383, 2019.

907 Rey-Pommier, A., Chevallier, F., Ciais, P., Christoudias, T., Kushta, J., Georgiou, G., Violaris, A., Dubart, F., and Sciare, J.: Mapping
908 NO_x emissions in Cyprus using TROPOMI observations: evaluation of the flux-divergence scheme using multiple parameter
909 sets, *Environmental Science and Pollution Research*, 32, 1932-1951, 2025.

910 Schwandner, F. M., Gunson, M. R., Miller, C. E., Carn, S. A., Eldering, A., Krings, T., Verhulst, K. R., Schimel, D. S., Nguyen, H.
911 M., and Crisp, D.: Spaceborne detection of localized carbon dioxide sources, *Science*, 358, eaam5782, 2017.

912 Sheng, M., Hou, Y., Song, H., Ye, X., Lei, L., Ma, P., and Zeng, Z.-C.: Estimating anthropogenic CO₂ emissions from China's
913 Yangtze River Delta using OCO-2 observations and WRF-Chem simulations, *Remote Sensing of Environment*, 316, 114515,
914 2025.

915 Sun, K.: Derivation of emissions from satellite-observed column amounts and its application to TROPOMI NO₂ and CO
916 observations, *Geophysical Research Letters*, 49, e2022GL101102, 2022.

917 Sun, K., Li, L., Jagini, S., and Li, D.: A Satellite Data-Driven Framework to Rapidly Quantify Air Basin-Scale NO_x Emission and
918 Its Application to the Po Valley during the COVID-19 Pandemic, *Atmospheric Chemistry and Physics Discussions*, 2021, 1-
919 29, 2021.

920 Sun, K., Zhu, L., Cady-Pereira, K., Chan Miller, C., Chance, K., Clarisse, L., Coheur, P.-F., González Abad, G., Huang, G., and Liu,
921 X.: A physics-based approach to oversample multi-satellite, multispecies observations to a common grid, *Atmospheric*
922 *Measurement Techniques*, 11, 6679-6701, 2018a.

923 Sun, Y., Frankenberg, C., Jung, M., Joiner, J., Guanter, L., Köhler, P., and Magney, T.: Overview of Solar-Induced chlorophyll
924 Fluorescence (SIF) from the Orbiting Carbon Observatory-2: Retrieval, cross-mission comparison, and global monitoring for
925 GPP, *Remote sensing of Environment*, 209, 808-823, 2018b.

926 Team, M.: The Multi-resolution Emission Inventory Model for Climate and Air Pollution Research, MEIC Model [data set], 2012.

927 van Geffen, J., Eskes, H., Compennolle, S., Pinardi, G., Verhoelst, T., Lambert, J. C., Sneep, M., ter Linden, M., Ludwig, A.,
928 Boersma, K. F., and Veefkind, J. P.: Sentinel-5P TROPOMI NO₂ retrieval: impact of version v2.2 improvements and
929 comparisons with OMI and ground-based data, *Atmos. Meas. Tech.*, 15, 2037-2060, 10.5194/amt-15-2037-2022, 2022.

930 Veefkind, J. P., Aben, I., McMullan, K., Förster, H., De Vries, J., Otter, G., Claas, J., Eskes, H., De Haan, J., and Kleipool, Q.:
931 TROPOMI on the ESA Sentinel-5 Precursor: A GMES mission for global observations of the atmospheric composition for
932 climate, air quality and ozone layer applications, *Remote sensing of environment*, 120, 70-83, 2012.

933 Verhoelst, T., Compennolle, S., Pinardi, G., Lambert, J. C., Eskes, H. J., Eichmann, K. U., Fjæraa, A. M., Granville, J., Niemeijer,
934 S., Cede, A., Tiefengraber, M., Hendrick, F., Pazmiño, A., Bais, A., Bazureau, A., Boersma, K. F., Bognar, K., Dehn, A., Donner,
935 S., Elokhov, A., Gebetsberger, M., Goutail, F., Grutter de la Mora, M., Gruzdev, A., Gratsea, M., Hansen, G. H., Irie, H., Jepsen,
936 N., Kanaya, Y., Karagkiozidis, D., Kivi, R., Kreher, K., Levelt, P. F., Liu, C., Müller, M., Navarro Comas, M., PETERS, A. J. M.,
937 Pommereau, J. P., Portafaix, T., Prados-Roman, C., Puentedura, O., Querel, R., Remmers, J., Richter, A., Rimmer, J., Rivera
938 Cárdenas, C., Saavedra de Miguel, L., Sinyakov, V. P., Stremme, W., Strong, K., Van Roozendaal, M., Veefkind, J. P., Wagner,
939 T., Wittrock, F., Yela González, M., and Zehner, C.: Ground-based validation of the Copernicus Sentinel-5P TROPOMI NO₂
940 measurements with the NDACC ZSL-DOAS, MAX-DOAS and Pandonia global networks, *Atmos. Meas. Tech.*, 14, 481-510,
941 10.5194/amt-14-481-2021, 2021.

942 Wang, R., Tao, S., Ciais, P., Shen, H., Huang, Y., Chen, H., Shen, G., Wang, B., Li, W., and Zhang, Y.: High-resolution mapping of
943 combustion processes and implications for CO₂ emissions, *Atmospheric Chemistry and Physics*, 13, 5189-5203, 2013.

944 Wei, C.: Historical trend and drivers of China's CO₂ emissions from 2000 to 2020, *Environment, development and sustainability*,
945 26, 2225-2244, 2024.

946 Wu, D., Lin, J. C., Fasoli, B., Oda, T., Ye, X., Lauvaux, T., Yang, E. G., and Kort, E. A.: A Lagrangian approach towards extracting
947 signals of urban CO₂ emissions from satellite observations of atmospheric column CO₂ (XCO₂): X-Stochastic Time-Inverted
948 Lagrangian Transport model ("X-STILT v1"), *Geoscientific Model Development*, 11, 4843-4871, 2018.

949 Xing, Y., Han, G., Mao, H., He, H., Bo, Z., Gong, R., Ma, X., and Gong, W.: MAM-YOLOv9: A Multi-Attention Mechanism
950 Network for Methane Emission Facility Detection in High-Resolution Satellite Remote Sensing Images, *IEEE Transactions on*
951 *Geoscience and Remote Sensing*, 2025.

952 Xu, J., Guan, Y., Oldfield, J., Guan, D., and Shan, Y.: China carbon emission accounts 2020-2021, *Applied Energy*, 360, 122837,
953 2024.

954 Xu, M., Han, G., Pei, Z., Yu, H., Li, S., and Gong, W.: Advanced method for compiling a high-resolution gridded anthropogenic
955 CO₂ emission inventory at a regional scale, *Geo-spatial Information Science*, 28, 117-130, 2025a.

956 Xu, T., Zhang, C., and Liu, C.: Enhanced quantification of global carbon emitters using collocated OCO-3 CO₂ and NO₂
957 observations from twin polar-orbiting satellites, *Geophysical Research Letters*, 52, e2025GL116877, 2025b.

958 Yang, E. G., Kort, E. A., Ott, L. E., Oda, T., and Lin, J. C.: Using space-based CO₂ and NO₂ observations to estimate urban CO₂
959 emissions, *Journal of Geophysical Research: Atmospheres*, 128, e2022JD037736, 2023.

960 Ye, X., Lauvaux, T., Kort, E. A., Oda, T., Feng, S., Lin, J. C., Yang, E. G., and Wu, D.: Constraining fossil fuel CO₂ emissions from
961 urban area using OCO-2 observations of total column CO₂, *Journal of Geophysical Research: Atmospheres*, 125,
962 e2019JD030528, 2020.

963 Yi, J., Huang, Y., Pei, Z., and Han, G.: Urban area observing system (UAOS) simulation experiment using DQ-1 total column
964 concentration observations, *EGUsphere*, 2024, 1-40, 2024.

965 Yi, J., Huang, Y., Pei, Z., and Han, G.: Urban Area Observing System (UAOS) simulation experiment using DQ-1 total column
966 concentration observations, *Atmospheric Chemistry and Physics*, 25, 13687-13710, 2025.

967 Zhang, H., Han, G., Ma, X., Chen, W., Zhang, X., Liu, J., and Gong, W.: Robust algorithm for precise X CO₂ retrieval using single
968 observation of IPDA LIDAR, *Optics Express*, 31, 11846-11863, 2023.

969 Zhang, H., Han, G., Chen, W., Pei, Z., Liu, B., Liu, J., Zhang, T., Li, S., and Gong, W.: Validation Method for Spaceborne IPDA
970 LIDAR $\{X\} - \{C\} \{O\}_2$ Products via TCCON, *IEEE Journal of Selected Topics*
971 *in Applied Earth Observations and Remote Sensing*, 17, 16984-16992, 2024.

972 Zhang, Q., Boersma, K. F., Zhao, B., Eskes, H., Chen, C., Zheng, H., and Zhang, X.: Quantifying daily NO_x and CO₂ emissions
973 from Wuhan using satellite observations from TROPOMI and OCO-2, *Atmospheric Chemistry and Physics Discussions*, 2022,
974 1-18, 2022.

975 Zhang, X., Yang, H., Bu, L., Fan, Z., Xiao, W., Chen, B., Zhang, L., Liu, S., Wang, Z., and Liu, J.: Estimation of diurnal emissions
976 of CO₂ from thermal power plants using spaceborne integrated path differential absorption (IPDA) lidar, *Atmospheric*
977 *Chemistry and Physics*, 25, 6725-6740, 2025.

978 Zhang, Y., Han, G., Huang, Y., Wang, H., Zhang, H., Pei, Z., Pu, Y., Luo, H., Yi, J., and Shi, T.: Attributing GHG emissions to
979 individual facilities using multi-temporal hyperspectral images: Methodology and applications, *ISPRS Journal of*
980 *Photogrammetry and Remote Sensing*, 232, 937-956, 2026.

981 Zheng, B., Geng, G., Ciais, P., Davis, S. J., Martin, R. V., Meng, J., Wu, N., Chevallier, F., Broquet, G., and Boersma, F.: Satellite-
982 based estimates of decline and rebound in China's CO₂ emissions during COVID-19 pandemic, *Science advances*, 6, eabd4998,
983 2020.

984